

THE SPATIAL EXTENT OF (U)LIRGs IN THE MID-INFRARED I: THE CONTINUUM EMISSION

T. DÍAZ-SANTOS¹, V. CHARMANDARIS^{1,2}, L. ARMUS³, A. O. PETRIC³, J. H. HOWELL³, E. J. MURPHY³,
J. M. MAZZARELLA⁴, S. VEILLEUX⁵, G. BOTHUN⁶, H. INAMI³, P. N. APPLETON⁷, A. S. EVANS⁸, S. HAAN³,
J. A. MARSHALL³, D. B. SANDERS⁹, S. STIERWALT³, AND J. A. SURACE³

Draft version May 16, 2018

ABSTRACT

We present an analysis of the extended mid-infrared (MIR) emission of the Great Observatories All-Sky LIRG Survey (GOALS) sample based on 5 – 15 μm low resolution spectra obtained with the Infrared Spectrograph on *Spitzer*. We calculate the fraction of extended emission as a function of wavelength for the galaxies in the sample, FEE_λ , defined as the fraction of the emission which originates outside of the unresolved component of a source at a given distance. We find that the FEE_λ varies from one galaxy to another, but we can identify three general types of FEE_λ : one where FEE_λ is constant, one where features due to emission lines and polycyclic aromatic hydrocarbons (PAH) appear more extended than the continuum, and a third which is characteristic of sources with deep silicate absorption at 9.7 μm . More than 30% of the galaxies have a median FEE_λ larger than 0.5, implying that at least half of their MIR emission is extended. Luminous Infrared Galaxies (LIRGs) display a wide range of FEE in their warm dust continuum ($0 \lesssim FEE_{13.2\mu\text{m}} \lesssim 0.85$). The large values of $FEE_{13.2\mu\text{m}}$ that we find in many LIRGs suggest that the extended component of their MIR continuum emission originates in scales up to 10 kpc, and may contribute as much as the nuclear region to their total MIR luminosity. The mean size of the LIRG cores at 13.2 μm is 2.6 kpc. However, once the IR luminosity of the systems reaches the threshold of $L_{\text{IR}} \sim 10^{11.8} L_\odot$, slightly below the regime of Ultra-luminous Infrared Galaxies (ULIRGs), all sources become clearly more compact, with $FEE_{13.2\mu\text{m}} \lesssim 0.2$, and their cores are unresolved. Our estimated upper limit for the core size of ULIRGs is less than 1.5 kpc. Furthermore, our analysis indicates that the compactness of systems with $L_{\text{IR}} \gtrsim 10^{11.25} L_\odot$ strongly increases in those classified as mergers in their final stage of interaction. The $FEE_{13.2\mu\text{m}}$ is also related to the contribution of an active galactic nucleus (AGN) to the MIR emission. Galaxies which are more AGN-dominated are less extended, independently of their L_{IR} . We finally find that the extent of the MIR continuum emission is correlated with the far-IR *IRAS* $\log(f_{60\mu\text{m}}/f_{100\mu\text{m}})$ color. This enables us to place a lower limit to the area in a galaxy from where the cold dust emission may originate, a prediction which can be tested soon with the *Herschel* Space Telescope.

Subject headings: infrared: galaxies — galaxies: evolution — galaxies: interactions — galaxies: starburst — galaxies: active

1. INTRODUCTION

The discovery by the Infrared Astronomical Satellite (IRAS) of luminous and ultra-luminous infrared (IR) galaxies, the so called LIRGs and ULIRGs¹⁰, has

opened a new window in extragalactic astrophysics. Over the past 25 years, follow up ground-based and space-born observations of these optically faint systems (see Houck et al. 1984) have revealed much about their detailed physical properties as well as their contribution to the integrated energy production in the Universe (see Sanders & Mirabel 1996, and references therein). More specifically it has been shown that even though LIRGs and ULIRGs are not very common in the local Universe (Soifer & Neugebauer 1991), they contribute a substantial fraction of the energy at $z \sim 1 - 2$ (Pérez-González et al. 2005; Le Floc'h et al. 2005; Caputi et al. 2007). Furthermore, the more IR luminous systems tend to be more disturbed dynamically, show evidence of merging, and often harbor an active galactic nucleus (AGN). The leap in sensitivity provided by the *Spitzer* Space Telescope (Werner et al. 2004) and in particular the availability of deep mid-infrared (MIR) spectroscopy with the Infrared Spectrograph (IRS; Houck et al. 2004) enabled the detailed study of the properties of large nearby

¹ Department of Physics and Institute of Theoretical and Computational Physics, University of Crete, GR-71003, Heraklion, Greece: tanio@physics.uoc.gr

² IESL/Foundation for Research and Technology - Hellas, GR-71110, Heraklion, Greece and Chercheur Associé, Observatoire de Paris, F-75014, Paris, France

³ Spitzer Science Center, Caltech, MS 220-6, Pasadena, CA 91125

⁴ Infrared Processing & Analysis Center, MS 100-22, California Institute of Technology, Pasadena, CA 91125

⁵ Department of Physics and Astronomy, University of New York at Stony Brook, NY 11794-3800

⁶ Department of Physics, University of Oregon, Eugene, OR 97403

⁷ NASA Herschel Science Center, IPAC, MS 100-22, Caltech, Pasadena, CA 91125

⁸ Department of Astronomy, 530 McCormick Road, University of Virginia, Charlottesville, VA 22904

⁹ Institute for Astronomy, University of Hawaii, 2680 Woodlawn Drive, Honolulu, HI 96822

¹⁰ LIRGs are defined as systems displaying an infrared luminosity, L_{IR} , of: $10^{11} L_\odot \leq L_{\text{IR}[8-1000\mu\text{m}]} < 10^{12} L_\odot$; ULIRGs:

$$L_{\text{IR}[8-1000\mu\text{m}]} \geq 10^{12} L_\odot.$$

(i.e., Armus et al. 2007, Desai et al. 2007, Imanishi et al. 2008, Farrah et al. 2008; Pereira-Santaella et al. 2010) and more distant (Houck et al. 2005; Yan et al. 2005, 2007) samples of (U)LIRGs. It thus became evident that, given the diversity of the MIR spectra of LIRGs and even more of ULIRGs, these systems cannot be grouped in a common class of galaxies either in terms of their MIR and/or far-infrared (FIR) properties. A number of correlations between the MIR colors, strength of features due to polycyclic aromatic hydrocarbons (PAHs), and line emissions, with the dominant source of energy production or interaction stage of galaxies have been explored (Armus et al. 2007; Desai et al. 2007; Veilleux et al. 2009, Petric et al. 2010). It appears that systems which are AGN dominated show weak PAH features, which are also correlated with the FIR spectral slope. Systems with greater MIR luminosity display weaker PAH emission, while dust extinction, quantified by the $9.7\mu\text{m}$ silicate feature, varies in strength and does not correlate with starburst or AGN dominated systems.

Recently, some studies have suggested that $z \sim 2$ ULIRGs are not just the analogs of local ULIRGs but instead they display MIR spectral features more similar to those seen in local, lower luminosity starburst galaxies and LIRGs (Farrah et al. 2008; Rigby et al. 2008). Some high- z sub-millimeter galaxies (SMGs) with IR luminosities similar to or greater than ULIRGs also show IR properties different from local ULIRGs (Pope et al. 2008; Murphy et al. 2009; Menéndez-Delmestre et al. 2009). All this evidence, in combination with results obtained from spatially resolved $H\alpha$ imaging and CO and radio maps of SMGs, suggest that the star formation (SF) taking place in ULIRGs and some SMGs at high redshift may be occurring over large areas, extending over several kpc across their disks (Bothwell et al. 2010; Ivison et al. 2010; Alexander et al. 2010). This is in contrast to what is seen in local ULIRGs where the strong bursts of SF are concentrated within the central kpc of galaxies probably due to interactions and mergers (Sanders & Mirabel 1996, Downes & Solomon 1998, Bryant & Scoville 1999, Soifer et al. 2000), which efficiently drive gas and dust towards their nuclei.

Here we present the first part of an analysis which has as the main goal to quantify the amount of extended MIR emission as a function of wavelength of a large sample of local LIRGs and ULIRGs which can be spatially resolved with *Spitzer*/IRS. This will provide extra evidence on the issue of whether the SF observed in high-redshift ultra-luminous systems has the same MIR characteristics to those observed in disks of lower IR luminosity local systems and it will allow us to examine whether the high- z systems are scaled-up versions in size, SF efficiency and therefore in IR luminosity of local LIRGs or ULIRGs. In this first paper, we study how the extended MIR *continuum* emission relates to global properties, such as the IR luminosity, AGN fraction, merging state, and FIR colors of the galaxies, and derive general trends for the entire sample. In a forthcoming paper (Díaz-Santos et al. 2010b, in preparation) we will address how the extended emission varies as function of other 5 to $15\mu\text{m}$ features, such as PAHs, and emission lines, and how it is linked to the particular physical properties of each galaxy.

The paper is structured as follows: In Section 2 we present our sample, the data reduction, and a summary

of the analysis we performed, in order to calculate the extended emission as a function of wavelength for each source. In Section 3 we explore possible correlation of the extended emission with the IR luminosity, stage of interaction, AGN strength and FIR colors for our sample, and discuss some implications for the high-redshift SMG population. The conclusions are presented in Section 4, while in the Appendix we provide more details on the analysis of the spatial profiles and the various tests performed in order to ascertain its robustness.

2. OBSERVATIONS AND DATA ANALYSIS

2.1. The sample

The sample on which we base our analysis is the Great Observatories All-Sky LIRG Survey (GOALS; Armus et al. 2009). GOALS comprises a complete, flux-limited sample of galaxies in the local Universe drawn from the Revised Bright Galaxy Sample (RBGS, Sanders et al. 2003) selected to be systems in the (U)LIRG luminosity class. Armus et al. (2009) describe in detail the characteristics of the GOALS sample and Petric et al. (2010) presents a comprehensive statistical analysis of the MIR spectral features as probed with *Spitzer*/IRS. Using a number of MIR diagnostics, Petric et al. (2010) estimate the AGN contribution to the MIR luminosity of the systems and, based on their apparent morphology, classify each galaxy into a stage of interaction (from isolated systems to advanced mergers). *Hubble Space Telescope (HST)* high spatial resolution optical and near-IR imaging for a fraction of the GOALS sample is presented by Haan et al. (2010). We refer the reader to these papers for further details. Out of the 291 galaxies (202 systems) included in the GOALS sample (see Armus et al. 2009), a total of 221 are used for this study. This is the number of *individual* galaxies for which IRS staring observations are available. Figure 1a presents the distribution of the galaxies as a function of their IR luminosity while Figure 1b shows it as a function of the distance. For reference, on the right panel we also indicate the projected linear scales that can be resolved at a given distance at $13.2\mu\text{m}$ using the IRS 5 – $15\mu\text{m}$ spectra.

The total IR luminosities of our systems were calculated using their *IRAS* flux densities and luminosity distances (see Armus et al. 2009, for details on the cosmology adopted), and following the prescription described in Sanders & Mirabel (1996). Since the spatial resolution of *Spitzer* is much higher than that of *IRAS*, there are MIPS $24\mu\text{m}$ *Spitzer* fluxes for 99 individual galaxies within multiple systems. For these, we distributed the L_{IR} of the system among the galaxies proportionally to their $24\mu\text{m}$ flux. For those systems without $24\mu\text{m}$ measurements of individual galaxies, the L_{IR} was evenly distributed among the members of the system. Due to this redistribution of the L_{IR} , there are now 35 galaxies with IR luminosities lower than $10^{11} L_{\odot}$ in our sample (see Figure 1b). In Table 1 we present the final L_{IR} and distance of the galaxies.

2.2. *Spitzer*/IRS Observations

All galaxies in GOALS have been observed in staring and/or mapping mode with the *Spitzer*/IRS instrument using all instrument modules (SL, LL, SH and

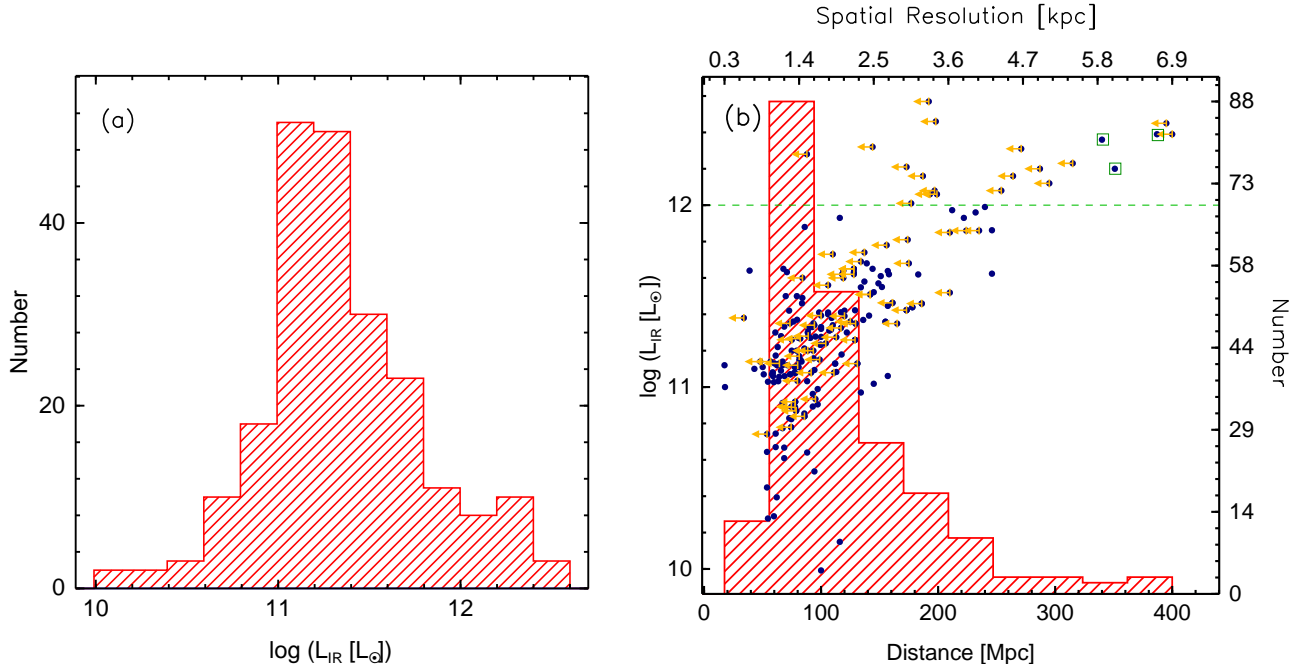


Figure 1. Histograms of the GOALS galaxy sample. (a) Distribution in IR luminosity; (b) Distribution in distance, indicated on the right y-axis. The upper x-axis displays the projected linear scale that can be resolved at $13.2\ \mu\text{m}$ at a given distance with IRS. The blue dots are the actual datapoints, with their L_{IR} indicated on the left y-axis of the plot. Upper limits in the x-axis value of a galaxy imply that its “core” is unresolved (see Section 3.2 and Figure 4). The green dashed line marks the boundary between LIRGs and ULIRGs. Except of three special cases (green boxes; see also Figure 4), all ULIRGs have unresolved cores independently of their distance.

LH). They also have IRAC (Fazio et al. 2004) and MIPS (Rieke et al. 2004) imaging observations at all bandpasses (Mazzarella & et al. 2010). The analysis presented in this paper is based on IRS SL staring observations covering the 5 to $\sim 15\ \mu\text{m}$ wavelength range with a spectral resolution of $R \sim 60 - 130$. As mentioned earlier, the aim of the study is to separate and quantify the extended emission of (U)LIRGs from the contribution of the unresolved nuclear component. Thus we limit our study to the shortest wavelengths where the spatial resolution of IRS ($\sim 3''.6$ at $13.2\ \mu\text{m}$) is sufficient to separate regions of physical scales that range from 0.22 kpc at the distance of the closest LIRG ($\sim 12\ \text{Mpc}$), to 6.1 kpc at $\sim 340\ \text{Mpc}$ where the farthest ULIRG of the sample is located (see Figure 1). The median distance of our galaxy sample is 91 Mpc, at which the spatial resolution is 1.7 kpc (also at $13.2\ \mu\text{m}$). In order to test the validity of some of the results obtained from the IRS SL spectroscopy, we also used the $8\ \mu\text{m}$ IRAC imaging (see Appendix and Mazzarella & et al. 2010 for details).

2.3. Data Reduction

As explained in Petric et al. (2010), all data were reduced using the S15, S16 and S17 IRS pipelines at the *Spitzer* Science Center¹¹. The pipelines were changed to modify certain header keywords, produce new flat-fields, and lower SL and LL fringes by 1-20%, provide better treatment of ramp slopes. The changes made between the pipelines should not systematically alter the measurements presented here. The reduction includes ramp fitting, dark sky subtraction, droop correction, linearity

correction and wavelength and flux calibration.

The backgrounds in the high resolution data were subtracted for all objects with dedicated sky observations ($\sim 60\%$ of the sources). For the low-resolution data without dedicated background observations, off-source nod were used for sky subtraction. Large objects in PID 30323 had dedicated background pointings. Bad pixel mask files were combined such that the final masks flagged all the individual bad pixels, if they were marked as bad in one individual exposure. Basic calibrated data sets (BCDs) for each nod were combined by determining the median if more than 5 BCDs were available, otherwise the average was used with 3-sigma clipping.

Each nod was extracted with SPICE¹² using the standard extraction aperture and point-source calibration. Nod 1 and nod 2 were compared with each other, and pixels were flagged if the difference between nod 1 and nod 2 exceeded 30%, and when adjacent pixels within the same nod differed by more than 30% (due to a cosmic ray or hot pixel).

2.4. Analysis

In this subsection we briefly summarize how, using 5– $15\ \mu\text{m}$ *Spitzer*/IRS SL staring observations, we can estimate the fraction of the extended emission of the galaxies as a function of wavelength (FEE_λ). More technical details of our analysis, as well as information on the specific treatment of the IRS data, are provided in the Appendix.

We commence the analysis with the 2 dimensional co-added files of the GOALS sample reduced as described

¹¹ See <http://ssc.spitzer.caltech.edu/irs>

¹² See <http://ssc.spitzer.caltech.edu/postbcd/doc/spice.pdf>

above (see Petric et al. 2010). We use the exact algorithms of the SSC pipeline, as well as the grid mapping of the slits on the IRS detector identified by the pseudo-rectangles of the “wavesamp” file to extract the spatial profiles of each source along the slit as a function of wavelength for each order and nod position. We follow the same approach to obtain the spatial profiles of a standard star (HR7341; PID: 1432) that we use as the reference point spread function (PSF) of an unresolved source.

For each wavelength resolution element, we fit the spatial profiles of the stellar PSF and the galaxy with Gaussian functions in order to calculate their peaks of emission and FWHMs. The FWHM of the Gaussian used to fit the galaxy profile is what we call the galaxy “core” size (see below). We then scale the peak of the spatial profile of the stellar PSF to the maximum of the spatial profile of the galaxy and subtract it. What remains is the spatial profile of the extended emission of the galaxy at a given wavelength. This extended emission (EE_λ) divided by the integrated emission of the galaxy all along the slit, is what we define as the fraction of extended emission as a function of wavelength, FEE_λ . We refer the reader to the Appendix for a more detailed explanation on its rather challenging calculation and the corrections that have to be applied to obtain reliable values. So formally:

$$FEE_\lambda = \frac{EE_\lambda}{E_\lambda(\text{total})} \quad (1)$$

where FEE_λ , EE_λ and $E_\lambda(\text{total})$ are the fraction of extended emission (ranging from zero to unity), the extended emission, and the total emission of the galaxy at a given wavelength respectively. Note that since we are scaling the stellar PSF to the maximum of the spatial profile of the galaxy, we implicitly assume that its nuclear emission is entirely produced by the central unresolved component. Therefore the values of EE_λ and the FEE_λ calculated in this manner are lower limits to the true extended emission. We report as the final FEE_λ at a given wavelength the average of the values obtained for each one of the two nod positions of the IRS slits. Comparing the difference between the two nods, we calculate the statistical uncertainty of the FEE_λ . The final uncertainty includes additional sources of error and depends on the details of the target (see Appendix for more information). For reference, the typical uncertainty on the FEE is between 0.05 and 0.15 (see Table 1).

Since the size of the IRS slit used projected on the galaxies does not entirely cover the size of the emitting region, we visually inspected their corresponding IRAC $8\ \mu\text{m}$ images in order to examine whether the slit was placed systematically along a privilege direction over the disk of the galaxies. We found that, most likely due to the large size of our sample, the position angle of the slit was randomly distributed along different directions on the galaxies and was not oriented systematically along bars, spiral arms or regions of enhanced star formation. As a consequence, variations in the intrinsic inclinations of the disks in more extended systems do not bias our findings.

3. RESULTS

The fraction of the extended emission as a function of wavelength, FEE_λ , calculated for each one of the

sources, contains a wealth of information. In the present section we discuss the types of FEE_λ we typically see in our sample, as well as the properties of the extended emission in the MIR continuum. For the latter we use as reference the resolution element at $13.2\ \mu\text{m}$ ($FEE_{13.2\ \mu\text{m}}$), as it is an area of the spectrum which is devoid of known emission or absorption features. Our findings though are similar for the $5 - 15\ \mu\text{m}$ MIR continuum in general¹³. A detailed comparison of the FEE_λ for different MIR spectral features (e.g., PAHs, emission lines or the $9.7\ \mu\text{m}$ silicate absorption feature) and the correlation of their ratios with the characteristics of each galaxy (e.g., nuclear and total extinction, presence of an AGN) will be addressed in a companion paper (Díaz-Santos et al. 2010b, in preparation). In addition, we construct spectra for the nuclear and extended components of galaxies as a function of the FEE_λ types (see next section). Table 1 presents the $FEE_{13.2\ \mu\text{m}}$ values for the galaxies in our sample, their “core” size at the same wavelength (see previous section and Appendix), and their $IRAS \log(f_{60\ \mu\text{m}}/f_{100\ \mu\text{m}})$ ratio, as well as other basic characteristics.

3.1. Types of FEE_λ Profiles

If one ignores projection effects or details on the intrinsic geometry of a source, the spatial profile of a galaxy as a function of wavelength, and consequently the estimated FEE_λ , depends primarily on the origin of the emission within the galaxy. The MIR continuum emission, PAH features, emission lines, as well as absorption features do not always originate from the same physical regions. Therefore it is reasonable to expect that the FEE_λ function varies among the galaxies. We find three different FEE_λ types, whose shapes are similar among the galaxies examined here. We exclude from this study 8 sources (4% of the sample) that appear practically unresolved in the $5 - 15\ \mu\text{m}$ range and for which their $FEE_\lambda \simeq 0$. We also exclude 11 galaxies (5% of the sample) whose FEE_λ could not be classified in any of the three types.

- Constant/featureless: 111 (50%) (U)LIRGs display a constant FEE_λ across the whole IRS $5 - 15\ \mu\text{m}$ wavelength range (see Figure 2, left panel). No MIR feature appears more extended than another or even than the continuum emission. This implies that there is no differentiation in the spatial distribution of the type of emitting region along the IRS slit. These constant FEE_λ functions range between ~ 0.1 up to ~ 0.85 among the galaxies of this type. A representative member of this type is NGC 3110 that, in particular, have a constant FEE_λ of ~ 0.65 .
- PAH- and line-extended: 37 galaxies (17%) of the sample show MIR features which are clearly more extended than the continuum emission (see Figure 2, central panel). More than $\sim 20\%$ of the flux detected in several PAH features and emission lines is extended, and in some sources it can be as high as 70%. In these type of galaxies, the bulk of

¹³ Note that this does not hold when the emission at $\sim 24\ \mu\text{m}$ is examined since the slit width of the IRS LL module is $10''5$, nearly three times worse than that of the SL (A. Petric, private communication).

Table 1
Properties Of The Sample

Galaxy name (1)	R.A. (J2000) (2)	Declination (J2000) (3)	Distance [Mpc] (4)	$\log L_{\text{IR}}$ [L_{\odot}] (5)	$FEE_{13.2\mu\text{m}}$ (6)	Core Size [kpc] (7)	IRAS $\log(f_{60\mu\text{m}}/f_{100\mu\text{m}})$ (8)
NGC0023	00h 09m 53.4s	+25° 55m 27s	65.2	11.12	0.67 ± 0.03	2.62 ± 0.02	-0.239 ± 0.004
MCG-02-01-051	00h 18m 50.9s	-10° 22m 36s	117.5	11.18	0.28 ± 0.06	2.28 ± 0.02	-0.111 ± 0.007
ESO350-IG038	00h 36m 52.5s	-33° 33m 17s	89.0	11.28	0.07 ± 0.08	1.57 ± 0.01*	0.135 ± 0.003
NGC0232	00h 42m 45.8s	-23° 33m 41s	95.2	11.28	0.37 ± 0.06	2.09 ± 0.01	...
NGC0232	00h 42m 52.8s	-23° 32m 27s	95.2	10.93	0.15 ± 0.07	1.79 ± 0.01*	...
MCG+12-02-001	00h 54m 03.9s	+73° 05m 05s	69.8	11.50	0.42 ± 0.06	1.65 ± 0.01	-0.123 ± 0.006
NGC0317B	00h 57m 40.4s	+43° 47m 32s	77.8	10.89	0.19 ± 0.09	1.46 ± 0.01*	-0.172 ± 0.005
MCG-03-04-014	01h 10m 08.9s	-16° 51m 10s	144.0	11.65	0.53 ± 0.05	4.16 ± 0.05	-0.154 ± 0.007
ESO244-G012	01h 18m 08.2s	-44° 28m 00s	91.5	11.08	0.15 ± 0.06	1.68 ± 0.01*	-0.103 ± 0.004
CGCG436-030	01h 20m 02.6s	+14° 21m 42s	134.0	11.69	0.02 ± 0.07	2.41 ± 0.02*	0.044 ± 0.008
ESO353-G020	01h 34m 51.3s	-36° 08m 14s	68.8	11.06	0.47 ± 0.06	1.72 ± 0.02	-0.336 ± 0.004
ESO297-G011	01h 36m 23.4s	-37° 19m 18s	74.6	10.82	0.52 ± 0.05	1.97 ± 0.03	...
ESO297-G011	01h 36m 24.1s	-37° 20m 25s	74.6	10.89	0.07 ± 0.07	1.35 ± 0.01*	...
IRASF01364-1042	01h 38m 52.8s	-10° 27m 12s	210.0	11.85	0.01 ± 0.08	3.79 ± 0.17*	-0.017 ± 0.008
IRASF01417+1651	01h 44m 30.6s	+17° 06m 09s	119.0	11.64	0.45 ± 0.05	2.74 ± 0.22	-0.033 ± 0.005
NGC0695	01h 51m 14.4s	+22° 34m 55s	139.0	11.68	0.73 ± 0.03	6.69 ± 0.09	-0.252 ± 0.006
UGC01385	01h 54m 53.8s	+36° 55m 04s	79.8	11.03	0.21 ± 0.06	1.51 ± 0.02*	-0.123 ± 0.006
NGC0838	02h 09m 42.8s	-10° 11m 02s	53.8	10.74	0.07 ± 0.06	0.96 ± 0.01*	...
NGC0838	02h 09m 38.7s	-10° 08m 47s	53.8	10.64	0.58 ± 0.04	1.65 ± 0.02	...
NGC0838	02h 09m 20.9s	-10° 07m 59s	53.8	10.45	0.73 ± 0.03	2.70 ± 0.05	...
NGC0828	02h 10m 09.5s	+39° 11m 24s	76.3	11.36	0.72 ± 0.03	3.49 ± 0.02	-0.344 ± 0.003
IC0214	02h 14m 05.6s	+05° 10m 23s	129.0	11.42	0.70 ± 0.04	5.82 ± 0.15	-0.210 ± 0.006
NGC0877	02h 17m 59.7s	+14° 32m 38s	54.6	11.03	0.80 ± 0.06	4.79 ± 1.32	...
NGC0877	02h 17m 53.3s	+14° 31m 18s	54.6	10.28	0.32 ± 0.05	1.09 ± 0.02	...
MCG+05-06-036	02h 23m 22.0s	+32° 11m 48s	145.0	11.52	0.25 ± 0.06	2.93 ± 0.03	...
MCG+05-06-036	02h 23m 19.0s	+32° 11m 18s	145.0	11.02	0.53 ± 0.06	3.96 ± 0.19	...
UGC01845	02h 24m 08.0s	+47° 58m 12s	67.0	11.12	0.53 ± 0.05	1.88 ± 0.01	-0.177 ± 0.020
NGC0992	02h 37m 25.5s	+21° 06m 02s	58.0	11.07	0.76 ± 0.03	3.26 ± 0.03	-0.166 ± 0.005
UGC02238	02h 46m 17.4s	+13° 05m 44s	92.4	11.33	0.68 ± 0.03	3.64 ± 0.04	-0.283 ± 0.004
IRASF02437+2122	02h 46m 39.1s	+21° 35m 10s	98.8	11.15	0.06 ± 0.09	1.77 ± 0.04*	-0.053 ± 0.029
UGC02369	02h 54m 01.8s	+14° 58m 36s	136.0	11.37	0.47 ± 0.05	3.52 ± 0.03	-0.142 ± 0.008
UGC02608	03h 15m 01.5s	+42° 02m 08s	100.0	11.39	0.17 ± 0.06	1.81 ± 0.02*	...
UGC02608	03h 15m 14.6s	+41° 58m 50s	100.0	9.99	0.49 ± 0.14	3.46 ± 1.69	...
NGC1275	03h 19m 48.2s	+41° 30m 42s	75.0	11.26	0.00 ± 0.06	1.27 ± 0.02*	-0.013 ± 0.028
IRASF03217+4022	03h 25m 05.4s	+40° 33m 32s	100.0	11.33	0.37 ± 0.06	2.21 ± 0.05	-0.163 ± 0.013
NGC1365	03h 33m 36.4s	-36° 08m 25s	17.9	11.00	0.48 ± 0.04	0.43 ± 0.01	-0.245 ± 0.000
IRASF03359+1523	03h 38m 47.1s	+15° 32m 54s	152.0	11.55	0.64 ± 0.04	6.15 ± 0.68	-0.086 ± 0.008
CGCG465-012	03h 54m 07.7s	+15° 59m 24s	94.3	10.54	0.71 ± 0.04	4.52 ± 0.21	...
CGCG465-012	03h 54m 16.0s	+15° 55m 43s	94.3	11.09	0.57 ± 0.04	2.61 ± 0.05	...
IRAS03582+6012	04h 02m 33.0s	+60° 20m 41s	131.0	11.13	0.05 ± 0.10	2.30 ± 0.02*	...
IRAS03582+6012	04h 02m 32.0s	+60° 20m 38s	131.0	11.13	0.48 ± 0.05	3.39 ± 0.05	...
UGC02982	04h 12m 22.7s	+05° 32m 49s	74.9	11.20	0.70 ± 0.03	3.11 ± 0.08	-0.302 ± 0.008
ESO420-G013	04h 13m 49.7s	-32° 00m 25s	51.0	11.07	0.21 ± 0.07	0.98 ± 0.01	-0.184 ± 0.002
NGC1572	04h 22m 42.8s	-40° 36m 03s	88.6	11.30	0.41 ± 0.06	2.09 ± 0.02	-0.321 ± 0.003
IRAS04271+3849	04h 30m 33.1s	+38° 55m 47s	80.8	11.11	0.36 ± 0.05	1.74 ± 0.02	-0.200 ± 0.030
NGC1614	04h 33m 60.0s	-08° 34m 46s	67.8	11.65	0.30 ± 0.05	1.39 ± 0.01	-0.029 ± 0.006
UGC03094	04h 35m 33.8s	+19° 10m 18s	106.0	11.41	0.71 ± 0.03	4.53 ± 0.07	-0.306 ± 0.010
ESO203-IG001	04h 46m 49.6s	-48° 33m 30s	235.0	11.86	0.00 ± 0.07	4.16 ± 0.03*	0.037 ± 0.006
MCG-05-12-006	04h 52m 05.0s	-32° 59m 26s	81.3	11.17	0.08 ± 0.07	1.48 ± 0.02*	-0.082 ± 0.004
NGC1797	05h 07m 44.8s	-08° 01m 08s	63.4	11.03	0.29 ± 0.06	1.26 ± 0.01	-0.125 ± 0.005
CGCG468-002	05h 08m 19.7s	+17° 21m 47s	77.9	10.92	0.04 ± 0.09	1.38 ± 0.02*	...
CGCG468-002	05h 08m 21.2s	+17° 22m 08s	77.9	10.92	0.22 ± 0.07	1.51 ± 0.01	...
IRAS05083+2441	05h 11m 25.9s	+24° 45m 18s	99.2	11.23	0.38 ± 0.06	2.24 ± 0.01	-0.082 ± 0.024
IRASF05081+7936	05h 16m 46.4s	+79° 40m 13s	240.0	11.99	0.43 ± 0.07	6.01 ± 0.09	-0.263 ± 0.006
IRAS05129+5128	05h 16m 56.0s	+51° 31m 57s	120.0	11.42	0.22 ± 0.06	2.38 ± 0.02	-0.049 ± 0.018
IRASF05189-2524	05h 21m 01.4s	-25° 21m 46s	187.0	12.16	0.02 ± 0.09	3.24 ± 0.04*	0.049 ± 0.003
IRASF05187-1017	05h 21m 06.5s	-10° 14m 46s	122.0	11.30	0.23 ± 0.09	2.38 ± 0.06	-0.174 ± 0.004
IRAS05223+1908	05h 25m 16.7s	+19° 10m 47s	128.0	11.65	0.00 ± 0.06	2.16 ± 0.01*	-0.299 ± 0.055
MCG+08-11-002	05h 40m 43.7s	+49° 41m 41s	83.7	11.46	0.30 ± 0.07	1.69 ± 0.01	-0.248 ± 0.003
NGC1961	05h 42m 04.6s	+69° 22m 42s	59.0	11.06	0.76 ± 0.02	3.10 ± 0.11	-0.513 ± 0.005
UGC03351	05h 45m 48.0s	+58° 42m 03s	65.8	11.28	0.74 ± 0.03	3.02 ± 0.12	-0.315 ± 0.002
IRAS05442+1732	05h 47m 11.2s	+17° 33m 46s	80.5	11.27	0.25 ± 0.06	1.56 ± 0.01	-0.104 ± 0.009
IRASF06076-2139	06h 09m 45.7s	-21° 40m 24s	165.0	11.35	0.05 ± 0.11	2.96 ± 0.03*	-0.120 ± 0.010
UGC03410	06h 14m 29.6s	+80° 26m 59s	59.7	11.03	0.76 ± 0.03	3.26 ± 0.11	...
UGC03410	06h 13m 57.9s	+80° 28m 34s	59.7	10.29	0.74 ± 0.02	2.88 ± 0.09	...

Table 1
Properties Of The Sample

Galaxy name (1)	R.A. (J2000) (2)	Declination (J2000) (3)	Distance [Mpc] (4)	$\log L_{\text{IR}}$ [L_{\odot}] (5)	$FEE_{13.2\mu\text{m}}$ (6)	Core Size [kpc] (7)	IRAS $\log(f_{60\mu\text{m}}/f_{100\mu\text{m}})$ (8)
NGC2146	06h 18m 37.8s	+78° 21m 24s	17.5	11.12	0.65 ± 0.03	0.62 ± 0.01	-0.122 ± 0.001
ESO255-IG007	06h 27m 21.7s	-47° 10m 36s	173.0	11.42	0.17 ± 0.08	3.32 ± 0.02	...
ESO255-IG007	06h 27m 22.6s	-47° 10m 47s	173.0	11.42	0.52 ± 0.06	4.96 ± 0.19	...
ESO255-IG007	06h 27m 23.1s	-47° 11m 02s	173.0	11.42	0.27 ± 0.12	3.56 ± 0.22	...
ESO557-G002	06h 31m 47.2s	-17° 37m 16s	93.6	11.16	0.35 ± 0.07	1.98 ± 0.02	-0.151 ± 0.008
UGC03608	06h 57m 34.4s	+46° 24m 10s	94.3	11.34	0.28 ± 0.07	1.79 ± 0.01*	-0.148 ± 0.005
IRASF06592-6313	06h 59m 40.2s	-63° 17m 52s	104.0	11.24	0.12 ± 0.07	1.84 ± 0.02*	-0.117 ± 0.006
IRASF07027-6011	07h 03m 28.5s	-60° 16m 43s	141.0	11.39	0.36 ± 0.08	3.09 ± 0.08	-0.141 ± 0.006
NGC2342	07h 09m 18.1s	+20° 38m 10s	78.0	11.08	0.31 ± 0.06	1.54 ± 0.02	-0.494 ± 0.003
IRAS07251-0248	07h 27m 37.6s	-02° 54m 54s	400.0	12.39	0.07 ± 0.12	7.51 ± 0.08*	0.009 ± 0.022
NGC2388	07h 29m 04.6s	+33° 51m 38s	62.1	10.39	0.29 ± 0.05	1.23 ± 0.01	-0.167 ± 0.003
MCG+02-20-003	07h 35m 43.4s	+11° 42m 34s	72.8	10.83	0.29 ± 0.06	1.44 ± 0.01	-0.153 ± 0.004
IRAS08355-4944	08h 37m 01.9s	-49° 54m 29s	118.0	11.62	0.20 ± 0.08	2.25 ± 0.01*	0.071 ± 0.042
NGC2623	08h 38m 24.1s	+25° 45m 16s	84.1	11.60	0.11 ± 0.10	1.52 ± 0.01*	-0.037 ± 0.002
ESO432-IG006	08h 44m 27.2s	-31° 41m 50s	74.4	10.78	0.44 ± 0.06	1.79 ± 0.02	...
ESO432-IG006	08h 44m 28.9s	-31° 41m 30s	74.4	10.78	0.15 ± 0.06	1.35 ± 0.02*	...
ESO60-IG016	08h 52m 30.5s	-69° 01m 59s	210.0	11.52	0.18 ± 0.07	3.95 ± 0.03*	-0.030 ± 0.010
IRASF08572+3915	09h 00m 25.3s	+39° 03m 53s	264.0	12.16	0.00 ± 0.07	4.70 ± 0.01*	0.185 ± 0.014
IRAS09022-3615	09h 04m 12.7s	-36° 27m 01s	271.0	12.31	0.11 ± 0.12	5.09 ± 0.04*	0.021 ± 0.014
IRASF09111-1007	09h 13m 36.5s	-10° 19m 29s	246.0	11.86	0.20 ± 0.08	4.81 ± 0.06	...
IRASF09111-1007	09h 13m 38.9s	-10° 19m 19s	246.0	11.62	0.34 ± 0.08	5.19 ± 0.17	...
UGC04881	09h 15m 55.5s	+44° 19m 57s	178.0	11.44	0.33 ± 0.08	3.72 ± 0.12	...
UGC04881	09h 15m 54.7s	+44° 19m 50s	178.0	11.44	0.47 ± 0.06	4.12 ± 0.18	...
UGC05101	09h 35m 51.6s	+61° 21m 11s	177.0	12.01	0.15 ± 0.07	3.30 ± 0.01*	-0.232 ± 0.003
MCG+08-18-013	09h 36m 37.2s	+48° 28m 27s	117.0	11.33	0.17 ± 0.22	1.33 ± 1.69*	-0.171 ± 0.008
IRASF09437+0317	09h 46m 21.1s	+03° 04m 16s	92.9	10.89	0.65 ± 0.07	3.47 ± 0.33	...
IRASF09437+0317	09h 46m 20.3s	+03° 02m 44s	92.9	10.96	0.57 ± 0.09	2.84 ± 0.31	...
NGC3110	10h 04m 02.1s	-06° 28m 29s	79.5	11.37	0.65 ± 0.04	2.96 ± 0.04	-0.295 ± 0.002
IRASF10038-3338	10h 06m 04.7s	-33° 53m 05s	156.0	11.78	0.04 ± 0.10	2.73 ± 0.02*	0.036 ± 0.013
IRASF10173+0828	10h 20m 00.2s	+08° 13m 32s	224.0	11.86	0.00 ± 0.08	3.90 ± 0.19*	-0.019 ± 0.008
NGC3221	10h 22m 20.0s	+21° 34m 10s	65.7	11.09	0.83 ± 0.04	5.10 ± 1.06	-0.386 ± 0.003
NGC3256	10h 27m 51.3s	-43° 54m 14s	38.9	11.64	0.54 ± 0.04	1.05 ± 0.01	-0.047 ± 0.001
ESO264-G036	10h 43m 07.5s	-46° 12m 44s	100.0	11.32	0.68 ± 0.03	3.91 ± 0.14	-0.343 ± 0.018
ESO264-G057	10h 59m 01.7s	-43° 26m 25s	83.3	11.14	0.40 ± 0.06	1.79 ± 0.03	-0.330 ± 0.026
IRASF10565+2448	10h 59m 18.1s	+24° 32m 34s	197.0	12.08	0.06 ± 0.09	3.61 ± 0.02*	-0.094 ± 0.004
MCG+07-23-019	11h 03m 54.0s	+40° 51m 00s	158.0	11.62	0.61 ± 0.10	6.02 ± 1.13	-0.208 ± 0.005
CGCG011-076	11h 21m 12.2s	-02° 59m 02s	117.0	11.41	0.26 ± 0.08	2.36 ± 0.02	-0.196 ± 0.013
IC2810	11h 25m 45.1s	+14° 40m 36s	157.0	11.45	0.47 ± 0.05	3.72 ± 0.08	-0.224 ± 0.006
ESO319-G022	11h 27m 54.2s	-41° 36m 51s	80.0	11.12	0.07 ± 0.09	1.39 ± 0.02*	-0.093 ± 0.009
ESO440-IG058	12h 06m 51.9s	-31° 56m 59s	112.0	11.13	0.52 ± 0.05	3.06 ± 0.05	...
ESO440-IG058	12h 06m 51.7s	-31° 56m 46s	112.0	11.13	0.53 ± 0.06	2.79 ± 0.22	...
IRASF12112+0305	12h 13m 46.0s	+02° 48m 42s	340.0	12.36	0.50 ± 0.07	9.83 ± 0.22:	-0.063 ± 0.006
NGC4194	12h 14m 09.7s	+54° 31m 35s	43.0	11.10	0.45 ± 0.05	1.04 ± 0.01	-0.035 ± 0.002
ESO267-G030	12h 14m 12.8s	-47° 13m 42s	97.1	10.90	0.57 ± 0.04	2.90 ± 0.06	...
ESO267-G030	12h 13m 52.3s	-47° 16m 25s	97.1	10.99	0.28 ± 0.06	1.89 ± 0.03	...
IRAS12116-5615	12h 14m 22.1s	-56° 32m 32s	128.0	11.65	0.17 ± 0.07	2.43 ± 0.02*	-0.122 ± 0.017
IRASF12224-0624	12h 25m 03.9s	-06° 40m 51s	125.0	11.36	0.07 ± 0.10	2.16 ± 0.08*	-0.133 ± 0.008
Mrk231	12h 56m 14.3s	+56° 52m 24s	192.0	12.57	0.00 ± 0.07	3.34 ± 0.01*	0.015 ± 0.002
NGC4922	13h 01m 25.3s	+29° 18m 49s	111.0	11.08	0.04 ± 0.09	1.92 ± 0.01*	-0.072 ± 0.006
CGCG043-099	13h 01m 50.3s	+04° 20m 00s	175.0	11.68	0.12 ± 0.09	3.30 ± 0.05*	-0.186 ± 0.007
MCG-02-33-098	13h 02m 19.7s	-15° 46m 04s	78.7	10.87	0.04 ± 0.09	1.37 ± 0.01*	...
MCG-02-33-098	13h 02m 20.4s	-15° 45m 59s	78.7	10.87	0.39 ± 0.06	1.71 ± 0.04	...
ESO507-G070	13h 02m 52.4s	-23° 55m 17s	106.0	11.56	0.08 ± 0.11	1.90 ± 0.02*	-0.081 ± 0.005
IRAS13052-5711	13h 08m 18.7s	-57° 27m 30s	106.0	11.40	0.42 ± 0.05	2.51 ± 0.04	-0.252 ± 0.021
IC0860	13h 15m 03.5s	+24° 37m 07s	56.8	11.14	0.16 ± 0.06	1.02 ± 0.01*	-0.001 ± 0.003
IRAS13120-5453	13h 15m 06.4s	-55° 09m 22s	144.0	12.32	0.18 ± 0.07	2.68 ± 0.02*	-0.105 ± 0.002
VV250a	13h 15m 35.0s	+62° 07m 29s	142.0	11.51	0.05 ± 0.07	2.51 ± 0.01*	...
VV250a	13h 15m 30.7s	+62° 07m 45s	142.0	11.51	0.13 ± 0.11	2.70 ± 0.10*	...
UGC08387	13h 20m 35.4s	+34° 08m 22s	110.0	11.73	0.17 ± 0.06	2.11 ± 0.01	-0.156 ± 0.003
NGC5104	13h 21m 23.1s	+00° 20m 33s	90.8	11.27	0.45 ± 0.06	2.17 ± 0.04	-0.295 ± 0.005
MCG-03-34-064	13h 22m 24.5s	-16° 43m 42s	82.2	11.27	0.01 ± 0.07	1.40 ± 0.01*	0.000 ± 0.010
NGC5135	13h 25m 44.0s	-29° 50m 00s	60.9	11.30	0.55 ± 0.05	1.77 ± 0.02	-0.264 ± 0.003
ESO173-G015	13h 27m 23.8s	-57° 29m 21s	34.0	11.38	0.25 ± 0.06	0.64 ± 0.01*	-0.089 ± 0.003
IC4280	13h 32m 53.4s	-24° 12m 25s	82.4	11.15	0.76 ± 0.02	4.40 ± 0.08	-0.307 ± 0.017
NGC5256	13h 38m 17.3s	+48° 16m 32s	129.0	11.26	0.36 ± 0.06	2.66 ± 0.02	...

Table 1
Properties Of The Sample

Galaxy name (1)	R.A. (J2000) (2)	Declination (J2000) (3)	Distance [Mpc] (4)	$\log L_{\text{IR}}$ [L_{\odot}] (5)	$FEE_{13.2\mu\text{m}}$ (6)	Core Size [kpc] (7)	$IRAS$ $\log(f_{60\mu\text{m}}/f_{100\mu\text{m}})$ (8)
NGC5256	13h 38m 17.8s	+48° 16m 41s	129.0	11.26	0.30 ± 0.23	2.47 ± 0.11*	...
NGC5257	13h 39m 57.7s	+00° 49m 53s	108.5	11.32	0.78 ± 0.03	9.60 ± 1.61	...
NGC5257	13h 39m 52.9s	+00° 50m 25s	108.5	11.32	0.82 ± 0.04	8.98 ± 1.29	...
Mrk273	13h 44m 42.1s	+55° 53m 13s	173.0	12.21	0.00 ± 0.06	3.10 ± 0.02*	-0.000 ± 0.002
UGC08739	13h 49m 13.9s	+35° 15m 26s	81.4	11.15	0.48 ± 0.04	1.92 ± 0.03	-0.438 ± 0.004
ESO221-IG010	13h 50m 56.9s	-49° 03m 18s	62.9	11.22	0.42 ± 0.06	1.40 ± 0.01	-0.231 ± 0.010
NGC5331	13h 52m 16.2s	+02° 06m 05s	155.0	11.36	0.62 ± 0.03	5.25 ± 0.10	...
NGC5331	13h 52m 16.4s	+02° 06m 30s	155.0	11.36	0.62 ± 0.07	5.45 ± 0.32	...
NGC5395	13h 58m 38.0s	+37° 25m 28s	58.7	11.08	0.68 ± 0.04	2.48 ± 0.42	...
NGC5395	13h 58m 33.6s	+37° 27m 12s	58.7	11.08	0.30 ± 0.05	1.18 ± 0.01	...
CGCG247-020	14h 19m 43.3s	+49° 14m 11s	120.0	11.39	0.04 ± 0.09	2.15 ± 0.02*	-0.149 ± 0.008
NGC5653	14h 30m 10.4s	+31° 12m 55s	60.2	11.13	0.76 ± 0.02	3.37 ± 0.05	-0.338 ± 0.002
IRASF14348-1447	14h 37m 38.3s	-15° 00m 24s	387.0	12.39	0.56 ± 0.05	12.37 ± 0.38:	-0.030 ± 0.009
IRASF14378-3651	14h 40m 59.0s	-37° 04m 32s	315.0	12.23	0.07 ± 0.12	5.78 ± 0.14*	-0.080 ± 0.012
NGC5734	14h 45m 09.0s	-20° 52m 13s	67.1	10.91	0.77 ± 0.03	3.96 ± 0.10	...
NGC5734	14h 45m 11.0s	-20° 54m 48s	67.1	10.77	0.65 ± 0.06	2.50 ± 0.16	...
VV340a	14h 57m 00.7s	+24° 37m 05s	157.0	11.64	0.76 ± 0.02	8.89 ± 0.18	...
VV340a	14h 57m 00.3s	+24° 36m 24s	157.0	11.06	0.67 ± 0.07	6.16 ± 0.57	...
VV705	15h 18m 06.1s	+42° 44m 44s	183.0	11.62	0.60 ± 0.11	6.37 ± 1.35	-0.045 ± 0.004
ESO099-G004	15h 24m 58.0s	-63° 07m 29s	137.0	11.74	0.20 ± 0.10	2.57 ± 0.04*	-0.122 ± 0.039
IRASF15250+3608	15h 26m 59.4s	+35° 58m 37s	254.0	12.08	0.01 ± 0.07	4.53 ± 0.04*	0.078 ± 0.008
NGC5936	15h 30m 00.8s	+12° 59m 22s	67.1	11.14	0.34 ± 0.04	1.33 ± 0.01	-0.306 ± 0.003
Arp220	15h 34m 57.2s	+23° 30m 11s	87.9	12.28	0.06 ± 0.12	1.53 ± 0.01*	-0.044 ± 0.001
NGC5990	15h 46m 16.4s	+02° 24m 55s	64.4	11.13	0.26 ± 0.06	1.22 ± 0.01*	-0.252 ± 0.005
NGC6090	16h 11m 40.8s	+52° 27m 27s	137.0	11.58	0.52 ± 0.04	3.90 ± 0.03	-0.162 ± 0.005
IRASF16164-0746	16h 19m 11.8s	-07° 54m 02s	128.0	11.62	0.14 ± 0.07	2.42 ± 0.02*	-0.109 ± 0.016
CGCG052-037	16h 30m 53.3s	+04° 04m 23s	116.0	10.15	0.36 ± 0.05	2.49 ± 0.02	-0.205 ± 0.005
NGC6156	16h 34m 52.6s	-60° 37m 08s	48.0	11.14	0.18 ± 0.05	0.86 ± 0.01*	-0.270 ± 0.012
ESO069-IG006	16h 38m 11.9s	-68° 26m 08s	212.0	11.97	0.44 ± 0.07	5.34 ± 0.03	-0.253 ± 0.010
IRASF16399-0937	16h 42m 40.1s	-09° 43m 13s	128.0	11.63	0.40 ± 0.07	2.76 ± 0.05	-0.243 ± 0.034
ESO453-G005	16h 47m 31.1s	-29° 21m 21s	100.0	11.28	0.62 ± 0.05	3.21 ± 0.19	-0.105 ± 0.040
NGC6240	16h 52m 58.9s	+02° 24m 03s	116.0	11.93	0.20 ± 0.06	2.26 ± 0.01	-0.062 ± 0.003
IRASF16516-0948	16h 54m 23.7s	-09° 53m 20s	107.0	11.31	0.73 ± 0.06	5.40 ± 0.66	-0.340 ± 0.027
NGC6286	16h 58m 31.6s	+58° 56m 13s	85.7	11.21	0.79 ± 0.02	6.66 ± 0.11	...
NGC6286	16h 58m 24.0s	+58° 57m 21s	85.7	10.85	0.56 ± 0.06	2.35 ± 0.12	...
IRASF17132+5313	17h 14m 20.4s	+53° 10m 31s	232.0	11.96	0.68 ± 0.04	9.89 ± 0.21	-0.114 ± 0.006
IRASF17138-1017	17h 16m 35.7s	-10° 20m 40s	84.0	11.49	0.69 ± 0.03	3.64 ± 0.06	-0.098 ± 0.008
IRASF17207-0014	17h 23m 22.0s	+00° 17m 01s	198.0	12.46	0.17 ± 0.06	3.75 ± 0.03*	-0.050 ± 0.007
ESO138-G027	17h 26m 43.3s	-59° 55m 55s	98.3	11.41	0.24 ± 0.09	1.90 ± 0.03	-0.064 ± 0.024
UGC11041	17h 54m 51.8s	+34° 46m 34s	77.5	11.11	0.61 ± 0.03	2.50 ± 0.05	-0.340 ± 0.003
CGCG141-034	17h 56m 56.6s	+24° 01m 01s	93.4	11.20	0.19 ± 0.09	1.75 ± 0.02*	-0.228 ± 0.010
IRAS17578-0400	18h 00m 31.8s	-04° 00m 53s	68.5	11.33	0.47 ± 0.05	1.71 ± 0.02	...
IRAS17578-0400	18h 00m 34.1s	-04° 01m 44s	68.5	10.61	0.54 ± 0.06	1.91 ± 0.15	...
IRAS17578-0400	18h 00m 24.3s	-04° 01m 03s	68.5	10.67	0.68 ± 0.04	2.77 ± 0.17	...
IRAS18090+0130	18h 11m 38.4s	+01° 31m 40s	134.0	11.55	0.53 ± 0.05	3.60 ± 0.06	...
IRAS18090+0130	18h 11m 33.4s	+01° 31m 42s	134.0	10.97	0.28 ± 0.09	2.65 ± 0.12	...
CGCG142-034	18h 16m 40.7s	+22° 06m 46s	88.1	11.03	0.37 ± 0.05	1.85 ± 0.03	...
CGCG142-034	18h 16m 33.8s	+22° 06m 38s	88.1	10.64	0.43 ± 0.05	2.04 ± 0.05	...
IRASF18293-3413	18h 32m 41.1s	-34° 11m 26s	86.0	11.88	0.50 ± 0.05	2.26 ± 0.02	-0.175 ± 0.003
NGC6670AB	18h 33m 34.2s	+59° 53m 17s	129.5	11.35	0.33 ± 0.05	2.68 ± 0.07	...
NGC6670AB	18h 33m 37.7s	+59° 53m 22s	129.5	11.35	0.21 ± 0.08	2.44 ± 0.02*	...
IC4734	18h 38m 25.8s	-57° 29m 25s	73.4	11.35	0.23 ± 0.06	1.37 ± 0.01*	-0.256 ± 0.003
NGC6701	18h 43m 12.5s	+60° 39m 11s	62.4	11.12	0.45 ± 0.05	1.52 ± 0.01	-0.300 ± 0.002
NGC6786	19h 10m 54.0s	+73° 24m 36s	113.0	11.08	0.53 ± 0.05	2.85 ± 0.08	...
NGC6786	19h 11m 04.4s	+73° 25m 32s	113.0	11.27	0.14 ± 0.11	2.06 ± 0.01*	...
ESO593-IG008	19h 14m 31.1s	-21° 19m 06s	222.0	11.93	0.53 ± 0.06	6.28 ± 0.13	-0.167 ± 0.003
IRASF19297-0406	19h 32m 22.3s	-04° 00m 01s	395.0	12.45	0.09 ± 0.09	7.51 ± 0.19*	-0.071 ± 0.024
IRAS19542+1110	19h 56m 35.8s	+11° 19m 04s	295.0	12.12	0.01 ± 0.08	5.43 ± 0.09*	-0.003 ± 0.022
ESO339-G011	19h 57m 37.6s	-37° 56m 08s	88.6	11.20	0.18 ± 0.07	1.60 ± 0.01*	-0.192 ± 0.015
NGC6907	20h 25m 06.6s	-24° 48m 32s	50.1	11.11	0.63 ± 0.04	1.69 ± 0.02	-0.321 ± 0.002
MCG+04-48-002	20h 28m 35.1s	+25° 44m 00s	64.2	11.06	0.45 ± 0.06	1.55 ± 0.02	-0.243 ± 0.006
NGC6926	20h 33m 06.1s	-02° 01m 38s	89.1	11.32	0.62 ± 0.05	2.49 ± 0.20	-0.307 ± 0.019
IRAS20351+2521	20h 37m 17.7s	+25° 31m 37s	151.0	11.61	0.43 ± 0.07	3.46 ± 0.06	-0.179 ± 0.010
CGCG448-020	20h 57m 24.1s	+17° 07m 35s	161.0	11.46	0.62 ± 0.04	5.68 ± 0.13	...
CGCG448-020	20h 57m 24.4s	+17° 07m 39s	161.0	11.46	0.08 ± 0.08	2.91 ± 0.01*	...

Table 1
Properties Of The Sample

Galaxy name (1)	R.A. (J2000) (2)	Declination (J2000) (3)	Distance [Mpc] (4)	$\log L_{\text{IR}}$ [L_{\odot}] (5)	$FEE_{13.2\mu\text{m}}$ (6)	Core Size [kpc] (7)	$IRAS$ $\log(f_{60\mu\text{m}}/f_{100\mu\text{m}})$ (8)
ESO286-IG019	20h 58m 26.8s	-42° 39m 00s	193.0	12.06	0.03 ± 0.09	3.41 ± 0.01*	0.073 ± 0.003
ESO286-G035	21h 04m 11.1s	-43° 35m 36s	79.1	11.20	0.60 ± 0.04	2.56 ± 0.03	-0.168 ± 0.006
IRAS21101+5810	21h 11m 29.3s	+58° 23m 07s	174.0	11.81	0.05 ± 0.08	3.20 ± 0.02*	-0.145 ± 0.039
ESO343-IG013	21h 36m 10.5s	-38° 32m 42s	85.8	10.84	0.49 ± 0.06	2.14 ± 0.06	...
ESO343-IG013	21h 36m 10.9s	-38° 32m 32s	85.8	10.84	0.01 ± 0.07	1.51 ± 0.02*	...
NGC7130	21h 48m 19.5s	-34° 57m 04s	72.7	11.42	0.35 ± 0.08	1.46 ± 0.04	-0.190 ± 0.002
ESO467-G027	22h 14m 40.0s	-27° 27m 50s	77.3	11.08	0.72 ± 0.03	3.57 ± 0.11	-0.350 ± 0.005
ESO602-G025	22h 31m 25.5s	-19° 02m 03s	110.0	11.34	0.36 ± 0.07	2.39 ± 0.02	-0.250 ± 0.005
UGC12150	22h 41m 12.2s	+34° 14m 56s	93.5	11.35	0.36 ± 0.05	1.98 ± 0.03	-0.289 ± 0.005
IRASF22491-1808	22h 51m 49.3s	-17° 52m 24s	351.0	12.20	0.21 ± 0.08	7.08 ± 0.28:	0.077 ± 0.009
NGC7469	23h 03m 15.6s	+08° 52m 25s	70.8	11.63	0.20 ± 0.06	1.37 ± 0.01	-0.109 ± 0.007
CGCG453-062	23h 04m 56.5s	+19° 33m 07s	109.0	11.38	0.69 ± 0.03	4.52 ± 0.24	-0.213 ± 0.007
ESO148-IG002	23h 15m 46.8s	-59° 03m 15s	199.0	12.06	0.02 ± 0.08	3.65 ± 0.02*	0.010 ± 0.004
IC5298	23h 16m 00.7s	+25° 33m 24s	119.0	11.60	0.02 ± 0.07	2.10 ± 0.01*	-0.122 ± 0.004
NGC7591	23h 18m 16.2s	+06° 35m 09s	71.4	11.12	0.34 ± 0.05	1.41 ± 0.02	-0.276 ± 0.010
ESO077-IG014	23h 21m 05.4s	-69° 12m 47s	186.0	11.46	0.14 ± 0.11	3.46 ± 0.07*	...
ESO077-IG014	23h 21m 03.7s	-69° 13m 00s	186.0	11.46	0.21 ± 0.09	3.60 ± 0.11	...
IRASF23365+3604	23h 39m 01.3s	+36° 21m 08s	287.0	12.20	0.09 ± 0.12	5.38 ± 0.14*	-0.083 ± 0.011
MCG-01-60-022	23h 42m 00.9s	-03° 36m 54s	100.0	11.23	0.43 ± 0.07	2.27 ± 0.05	-0.185 ± 0.007
IRAS23436+5257	23h 46m 05.4s	+53° 14m 01s	149.0	11.57	0.36 ± 0.09	3.13 ± 0.11	-0.202 ± 0.009
NGC7753	23h 47m 04.8s	+29° 29m 00s	73.6	11.07	0.31 ± 0.12	1.42 ± 0.10	...
NGC7753	23h 46m 58.6s	+29° 27m 32s	73.6	11.07	0.64 ± 0.04	2.68 ± 0.07	...
NGC7771	23h 51m 03.9s	+20° 09m 01s	61.2	10.74	0.56 ± 0.04	1.45 ± 0.04	...
NGC7771	23h 51m 24.8s	+20° 06m 42s	61.2	11.17	0.51 ± 0.04	1.66 ± 0.02	...
NGC7771	23h 51m 22.6s	+20° 05m 49s	61.2	10.67	0.43 ± 0.07	1.43 ± 0.07	...
Mrk0331	23h 51m 26.8s	+20° 35m 10s	79.3	11.50	0.37 ± 0.07	1.77 ± 0.02	-0.101 ± 0.004

Note. — (1) Galaxy name. Multiple systems are indicated with the same name but providing the right ascension and declination of the individual galaxies; (2) Right Ascension (J2000); (3) Declination (J2000); (4) Luminosity distance (see Armus et al. 2009, for details). The L_{IR} is accurate to within 0.01 dex (U et al. 2011, in preparation); (5) IR luminosity of the galaxy (see Section 2.1 for details on its calculation); (6) Fraction of extended emission at $13.2\mu\text{m}$ ($FEE_{13.2\mu\text{m}}$); (7) Size (FWHM) of the galaxy core at $13.2\mu\text{m}$ (see Appendix). The asterisks denote galaxies with unresolved cores (FWHM within 10% of that of the unresolved stellar PSF). The colons indicate galaxies whose IRS spectra has been contaminated by a close companion galaxy. In this cases, the $FEE_{13.2\mu\text{m}}$ and the core size are not reliable; (8) $IRAS$ $\log(f_{60\mu\text{m}}/f_{100\mu\text{m}})$ color. Values are given only for sources with a unique $IRAS$ color, i.e., not associated to two individual galaxies.

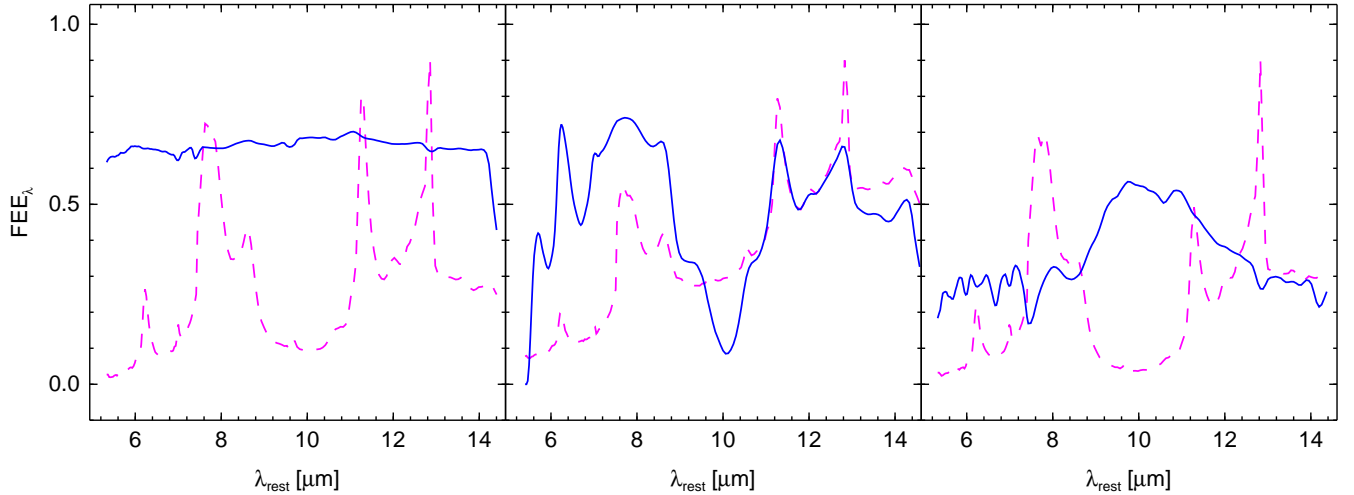


Figure 2. FEE_{λ} function of 3 galaxies that serve as examples of the 3 types identified in the sample (blue solid line). The spectrum of each galaxy, scaled to arbitrary units, is also plotted for reference (pink dashed line). The galaxies are: NGC 3110 (left), NGC 1365 (center), and MCG+08-11-002 (right). The FEE_{λ} functions have been smoothed with a 4-pixel box to reduce the noise. Left panel: Constant/featureless FEE_{λ} . Middle panel: PAH and line extended emission. Right panel: Silicate-extended emission.

the continuum emission originates from a circum-nuclear region more compact than that giving rise to the MIR spectral features. The fact that these two components of emission are spatially decoupled suggests that, contrary to the previous type of FEE_λ , different physical processes are responsible for the energy production in the nucleus and in the disk. This could be due to the presence of either an AGN or intense starburst in the nucleus producing a strong MIR continuum, compared to a more quiescent, star formation on the disk where older stellar populations may heat the gas and PAH molecules. A representative member of this type is NGC 1365.

- Silicate-extended: Another 54 (24%) galaxies of the sample show a rather interesting FEE_λ shape in which the maximum peaks around $10\ \mu\text{m}$ (see Figure 2, right panel). Inspecting the FEE_λ more closely, it appears that there is an increase between ~ 8 and $12\ \mu\text{m}$, around the wavelength range where the $9.7\ \mu\text{m}$ silicate absorption feature is present. We attribute this maximum to an extinction effect in these systems. Galaxies containing very obscured nuclei will show little or not at all “unresolved emission”, at wavelengths dominated by the silicate absorption feature. As mentioned earlier, we always normalize the spatial profile of an unresolved point source to the source profile at every wavelength and subtract it in order to determine the value of FEE_λ . Consequently, if the nucleus of a galaxy is very extinguished, any residual emission within the $9.7\ \mu\text{m}$ band, when compared to the emission at any other wavelength that is not affected by the absorption feature, would be interpreted as an excess in the fraction of extended emission originating from the outer disk of these galaxies, where the extinction is less extreme. This is reflected in the form of FEE_λ we compute, and implies that the silicate strength (i.e., the apparent optical depth) calculated from the integrated spectrum of these galaxies may not be representative of their nuclei (see Spoon et al. 2004). A representative member of this type is MCG+08-11-002.

The presence of these types of FEE_λ , suggest that the mechanism by which local (U)LIRGs produce the MIR emission in their disks and nuclear regions varies from one source to the next. There is a great diversity not only in the integrated spectrum of a LIRG/ULIRG, but also in the spatial distribution of the regions responsible for the formation of the various MIR features, such as PAHs, emission lines, and dust continuum. The FEE_λ measured indicates that in some galaxies the emission from PAHs, atomic or molecular lines is more extended than the dust continuum emission, while in others their extent is similar. These variations are clearly related to the location and intensity of the physical process producing the emission detected, such as young star clusters or an AGN. Our results suggest that not all local (U)LIRGs are to be a priori considered as compact, uniform MIR emitters. There has been an interesting such case reported already, VV114, a system with $L_{\text{IR}} = 4 \times 10^{11} L_\odot$ harboring an AGN, for which

high resolution ground-based MIR imaging (Soifer et al. 2001), as well as $5 - 15\ \mu\text{m}$ ISO/CAM spectral maps reveal that nearly 60% of the MIR emission is extended (Le Floch et al. 2002). This is understood since in these systems the MIR emission is not necessarily dominated by an AGN or a single burst of star formation. Moreover, in the cases of purely starburst-driven (U)LIRGs, the PAH and continuum emission may not be associated to the same star formation event but instead are probably excited, as a whole, by different stellar populations. For example the $11.3\ \mu\text{m}$ PAH emission is more representative of *recent* star formation event with ages greater than $8 - 10$ Myr, while *current* star formation, less than $8 - 10$ Myr in age, is better traced by the $[\text{Ne II}]12.81\ \mu\text{m}$ or MIR continuum emission (Díaz-Santos et al. 2010). In these galaxies, older star formation traced by PAH emission is more extended and is more typical of galactic disks, while recent star formation, associated to MIR continuum emission, is more compact and concentrated towards the nucleus.

3.2. The L_{IR} Dependence Of The Extended Emission

The histogram in Figure 3 presents the distribution of the median FEE_λ , calculated over the whole $5 - 15\ \mu\text{m}$ range, for all the galaxies in our sample (black histogram). 32% of the galaxies have a median FEE_λ larger than 0.5, that is, at least 50% of the MIR emission of these galaxies is extended. In addition, more than 90% of the galaxies have a median FEE_λ larger than 0.1.

High resolution MIR images of a handful of local (U)LIRGs have revealed rather compact emission originating from a few hundred parsecs around their nuclei (Soifer et al. 2000, 2001; Díaz-Santos et al. 2008). This trend is also present in our data, even though the physical scales we probe with *Spitzer* are larger. In Figure 3 we also show three histograms of the median FEE_λ for galaxies grouped in three ranges of IR luminosity. We note that galaxies with the $L_{\text{IR}} < 10^{11.25} L_\odot$ (red histogram) and $10^{11.25} L_\odot \leq L_{\text{IR}} < 10^{12} L_\odot$ (orange) display similar median values of their FEE_λ distributions. The median of each histogram is 0.46 and 0.39 respectively, which is in agreement with previous studies based on smaller samples of LIRGs (Pereira-Santaella et al. 2010). The median values of the low IR luminosity bins are very similar to that found for the median FEE_λ distribution of the whole sample of galaxies, 0.40. However, we find that the median of the corresponding distribution for ULIRGs (blue histogram) is only 0.14. A Kolmogorov-Smirnov (K-S) test comparing the two LIRG samples with that of the ULIRG indicates significance levels lower than 1×10^{-5} , implying that it is very unlikely that ULIRGs are drawn from the same parent distribution as LIRGs. Our data therefore suggest that, as a whole, the median FEE_λ of ULIRGs is 2 – 3 times lower than that of LIRGs.

We now explore whether the spatial extent of the MIR continuum of (U)LIRGs is a smooth function of their IR luminosity, or whether there is a certain L_{IR} above which their properties change drastically making their emission substantially more concentrated. The blue circles in Figure 4a show the FEE of the $13.2\ \mu\text{m}$ continuum emission ($FEE_{13.2\ \mu\text{m}}$) as a function of the L_{IR} for the galaxies in our sample. The size of the circles scales with their distance. As we can see, LIRGs display a wide

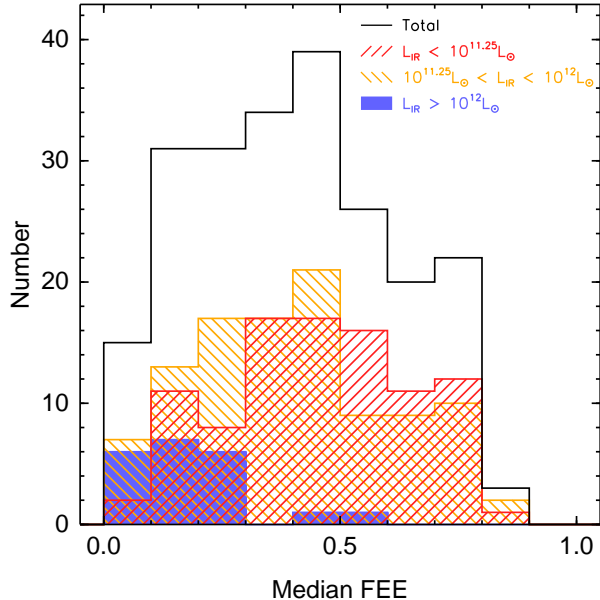


Figure 3. Histogram of the median FEE_λ (calculated over the 5–15 μm range) for the GOALS sample (black). The red and orange striped, and the blue solid histograms are the distributions of the median FEE_λ for galaxies with $L_{\text{IR}} < 10^{11.25} L_\odot$, $10^{11.25} L_\odot \leq L_{\text{IR}} < 10^{12} L_\odot$, and $L_{\text{IR}} > 10^{12} L_\odot$, respectively.

range of $FEE_{13.2\mu\text{m}}$. They vary from compact systems ($FEE_{13.2\mu\text{m}} \simeq 0$) to others which are very extended ($FEE_{13.2\mu\text{m}} \simeq 0.85$). No clear trend with L_{IR} is evident over the decade in IR luminosity covered by the LIRGs. However, if we examine the median value of the $FEE_{13.2\mu\text{m}}$ calculated in different luminosity bins (black line), this appears to decrease as the L_{IR} of the galaxies increases, going from $\simeq 0.5$ at $L_{\text{IR}} \simeq 10^{10.3} L_\odot$ to $\simeq 0.1$ at $L_{\text{IR}} \simeq 10^{12.3} L_\odot$. Moreover, for IR luminosities above $\sim 10^{11.8} L_\odot$, just below the nominal transition between LIRGs and ULIRGs, the maximum of the $FEE_{13.2\mu\text{m}}$ (upper dashed line) drops abruptly, and only a few galaxies have $FEE_{13.2\mu\text{m}}$ values larger than 0.2. Indeed, all ULIRGs are unresolved¹⁴ (see Figure 4b) and have $FEE_{13.2\mu\text{m}} \lesssim 0.2$.

One may consider that the decrease of the median $FEE_{13.2\mu\text{m}}$ with L_{IR} is due to the loss of spatial resolution (see Figure 4b and Figure 1b). The more luminous systems tend to be at larger distances and hence their unresolved nuclear component progressively accounts for a larger fraction of their total flux. This bias would affect our ability to measure large values of $FEE_{13.2\mu\text{m}}$ for distant sources as they become progressively unresolved. We define as unresolved those galaxies whose “core” angular sizes are within 10% of the stellar PSF, and indicate it as a dotted line in Figure 4b. At this point, it is important to differentiate between the core size of a galaxy,

¹⁴ There are three systems which deviate from this trend: ESO557-G002, IRAS03359+1523 and IRAS22491-1808. They are interacting systems and their IRAC 8 μm images show the presence of nearby companion galaxies affecting the spatial profiles estimated with the IRS slits. These three systems are marked with green boxes in Figures 1b and 4, and they are no longer considered in our analysis.

used to establish whether it is resolved or not, and its measured FEE . While the former is merely a Gaussian fit to the nuclear emission of the galaxy from which a FWHM is obtained, the latter also accounts for possible low surface brightness emission which is probably more extended than the core of the galaxy. As a consequence, sources classified as unresolved in Figure 4b, may still display non-zero $FEE_{13.2\mu\text{m}}$ values in Figure 4a.

If our ability to measure the FEE and the size of the MIR emitting region of the galaxies were totally dominated by the instrumental resolution, the fraction of unresolved sources would be a monotonically increasing linear function of distance. To examine this, we divided our sample in 3 distance bins at [25-75], [75-125] and [150-250] Mpc, each doubling the distance of the previous one, and calculated the fraction of unresolved sources in each one. We find that the corresponding fraction of unresolved sources is 16% (9/55), 33% (29/88) and 45% (18/40). That is, as the distance doubles, the fraction of unresolved sources nearly doubles. However, there are sources up to $\simeq 240$ Mpc, for which we can measure a $FEE_{13.2\mu\text{m}} \simeq 0.7$ independently of their L_{IR} , implying that we are able to resolve the extended emission at those distances if present.

Hence, the steep drop of the maximum value of $FEE_{13.2\mu\text{m}}$ above $L_{\text{IR}} \sim 10^{11.8} L_\odot$ can not be explained by a progressive increasing of the distance to the galaxies. We note that all 10 ULIRGs found at distances up to 200 Mpc, where we are still able to measure large values of $FEE_{13.2\mu\text{m}}$, are unresolved and display $FEE_{13.2\mu\text{m}} < 0.2$ (see Figure 4b). However, 68% (54/80) of LIRGs at similar distances, between 100 and 200 Mpc, have large $FEE_{13.2\mu\text{m}}$ reaching values up to 0.7. If ULIRGs were drawn from the same parent population as LIRGs, one would expect to resolve around 6 out of these 10 ULIRGs, which is not the case. Therefore, it appears that there is a real threshold in the distribution of the compactness of IR bright galaxies happening at $L_{\text{IR}} \sim 10^{11.8} L_\odot$, with higher luminosity systems being more compact.

When we examine only the LIRGs of our sample, we find that, independently of the distance, there are systems with more than 50% of their MIR continuum emission originating outside the unresolved central region. This implies that the extended emission in these systems is larger than the contribution of the nuclear region to their total MIR luminosity. In fact, we are able to resolve sizes (FWHMs) of LIRG cores up to ~ 10 kpc, much larger than the spatial resolution at any given distance. However, since our sample is flux-limited rather than distance-limited, it is quite challenging to ascertain a representative physical size for the sources in a given luminosity range. Both the FEE and the size of a source depend on whether we can resolve their emission. The resolution though is a function of the distance, and at the same time more luminous galaxies are seen at larger distances. Hence, upper limits on the sizes of sources also depends on their luminosities. If we simply compute the mean core size of LIRGs using only those systems that are resolved, which are found above the dotted line in Figure 4b, the result is 3.1 kpc, while the median is 2.7 kpc. A more thorough analysis can be performed us-

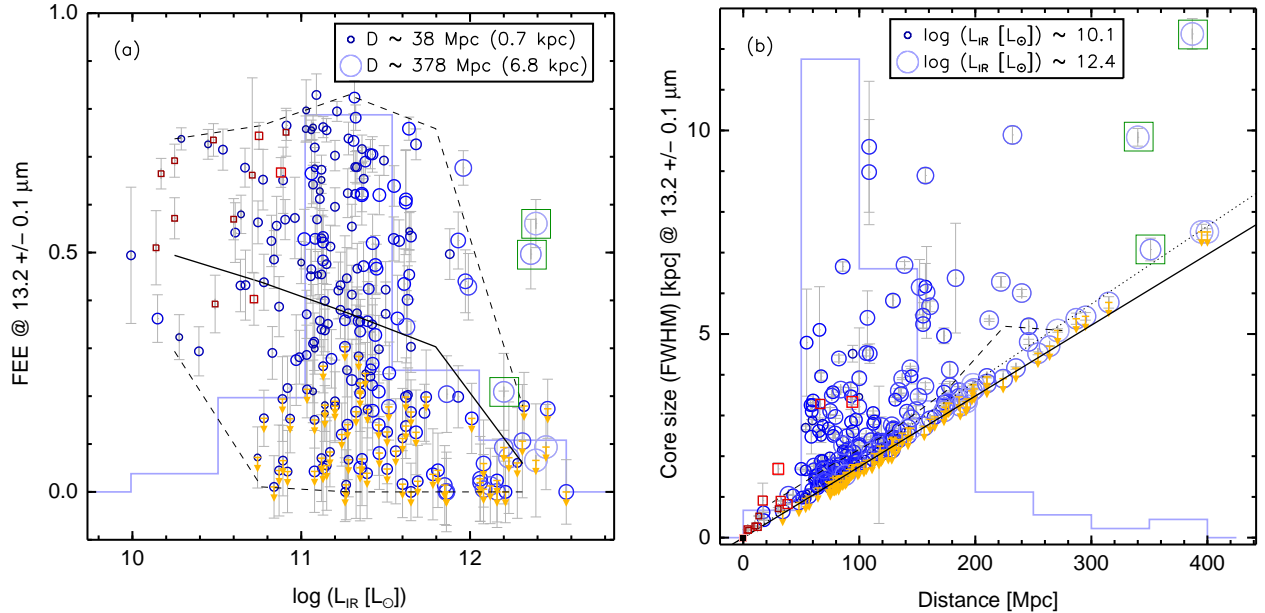


Figure 4. (a) Plot of the FEE of the continuum at $13.2\ \mu\text{m}$ as a function of the IR luminosity for the galaxies of our sample (blue circles). The size of the circles scales with the distance to the galaxy. The red squares in the left and right panels are the results obtained for a sub-sample of galaxies taken from the starburst sample of Brandl et al. (2006, see text for details). The size of the squares also scales with distance. For reference, the projected linear size of the unresolved component at the given distance is shown in parenthesis. The background faint (blue) line is a normalized histogram of the galaxies at different IR luminosity bins. The solid (black) line is the median of the $FEE_{13.2\mu\text{m}}$ at the different luminosity bins. The lower and upper dashed lines are the minimum and maximum $FEE_{13.2\mu\text{m}}$ at each bin respectively. The upper limits marked with orange arrows indicate galaxies whose core sizes are unresolved (see next). (b) Plot of the linear size of the galaxy core, measured as the FWHM of the Gaussian function fitted to the spatial profile at $13.2\ \mu\text{m}$, as a function of distance (see text and Appendix for details). As in (a), the size of the circles and squares scales with the IR luminosity of the source. The faint (blue) line is a normalized histogram of the galaxies at different distance bins. The solid line represents the size of an unresolved source, the FWHM of the stellar PSF, at $13.2\ \mu\text{m}$ as a function of distance. The black dashed line is the median size of galaxies in each distance bin. The black dotted line indicates the expected location of a galaxy with a core size 10% larger than that of the unresolved stellar PSF (solid line). The three systems which deviate from the main trend due to contamination of the MIR profile by a companion galaxy are marked with green boxes (see text).

ing the survival analysis package ASURV¹⁵, which properly takes into account the lower and/or upper limits in a given distribution. If we use this approach, we find that the mean core size of LIRGs at $13.2\ \mu\text{m}$ is $2.6 \pm 0.1\ \text{kpc}$.

Regarding the ULIRG sub-sample, establishing a typical size for the region from which their extended emission originates is even more challenging since all of them are unresolved. If we consider the ULIRGs located up to a distance of $\sim 100\ \text{Mpc}$ as the reference, we can estimate an upper limit for their core sizes of $\sim 1.5\ \text{kpc}$, which is agreement with previous findings (e.g., Soifer et al. 2001).

In order to put our results for the GOALS sample in the context of the less luminous but more numerous galaxies of our local universe, we have analyzed the low luminosity sources from the starburst sample of (Brandl et al. 2006). We selected galaxies with $L_{\text{IR}} \leq 10^{11}\ L_{\odot}$ where the IRS slit was well centered on their nuclei (see their Figure 1): IC 342, Mrk 52, NGC 520, NGC 660, NGC 1097, NGC 1222, NGC 3628, NGC 4088, NGC 4676, NGC 4945, NGC 7252 and NGC 7714. Our measurements are plotted as red squares in Figure 4a and b. We find that the $FEE_{13.2\mu\text{m}}$ of these systems ranges between $\sim 0.4 - 0.8$ and is within the values shown by

GOALS galaxies with similar IR luminosities. This suggests that the extent of the MIR continuum emission in starburst galaxies and in the low luminosity tail of the GOALS LIRGs is comparable.

Finally we should mention that our study provides no evidence that LIRGs with small $FEE_{13.2\mu\text{m}}$ have the highest IR luminosities since the most point-like sources do not appear to be systematically the most luminous in the $5 - 15\ \mu\text{m}$ range (see also Figure 3). Instead, as mentioned above, all LIRGs show the same scatter in the $FEE_{13.2\mu\text{m}}$ at any given distance. It is only above the threshold of $L_{\text{IR}} \sim 10^{11.8}\ L_{\odot}$ when we observe a significant reduction of the $FEE_{13.2\mu\text{m}}$ to values of $\lesssim 0.2$.

3.3. Dependence Of The Extended Emission On The Stage Of Interaction

We have shown that there is a strong evolution of the compactness of the continuum MIR emission at the transition point from LIRGs to ULIRGs. What is the physical process responsible for this? It is known that most ULIRGs are merging systems with clear signs of interactions (e.g., Clements et al. 1996; Murphy et al. 2001). Could it be that the merging processes in (U)LIRGs which drive the material of the galaxies to their nuclei causing massive star formation, is the same reason that makes them appear more compact in the MIR?

The galaxies were classified in 5 stages: (0) no obvious

¹⁵ The package ASURV is available at <http://astrostatistics.psu.edu/statcodes/asurv>

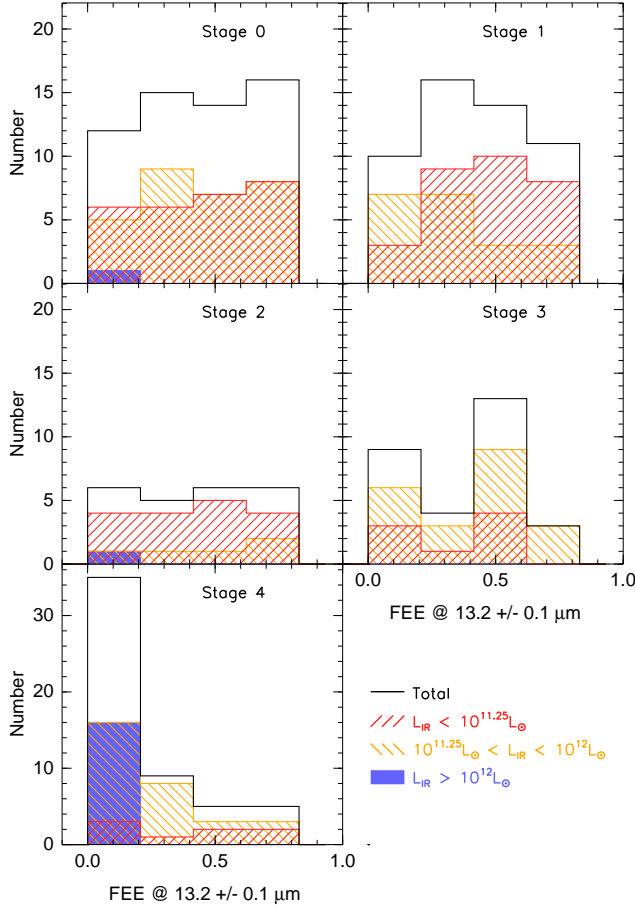


Figure 5. Histograms of the $FEE_{13.2\mu m}$ for the galaxies in our sample divided as a function of their merging stage as defined by Petric et al. (2010), from isolated - stage 0 - systems, to fully merged - stage 4 - galaxies (see Petric et al. 2010, for more details). The galaxies have been separated in different luminosity bins as in Figure 3. We exclude from this analysis the galaxies marked with green boxes in Figure 4 (see Section 3.2).

sign of disturbance in their IRAC or *HST* morphologies, or published evidence that the gas is in dynamical equilibrium (i.e., undisturbed circular orbits); (1) early stage, where the galaxies are within one arc-minute of each other, but little or no morphological disturbance can be observed; (2) the galaxies exhibit bridges, strong disturbance but they do not have a common envelope and each optical disk is relatively intact; (3) the optical disks are completely destroyed but 2 nuclei can be distinguished; (4) the two interacting nuclei are merged but structure in the disk indicates the source has gone through a merger. The classification was proposed by Petric et al. (2010) and it is based on Hubble Space Telescope (*HST*) imaging, $3.6\mu m$ *Spitzer* IRAC images as well as optical SDSS images of the objects (see also Surace 1998). In Figure 5 we plot total (black) histograms of the $FEE_{13.2\mu m}$ for each interaction stage, and also divided in 3 IR luminosity bins (red, orange and blue, as in Figure 3). We study 214 (out of the 221) galaxies for which the stage of merger is available. We observe that the most advanced mergers (stage 4) tend to have low $FEE_{13.2\mu m}$ values, i.e., they are more compact. K-S tests performed between

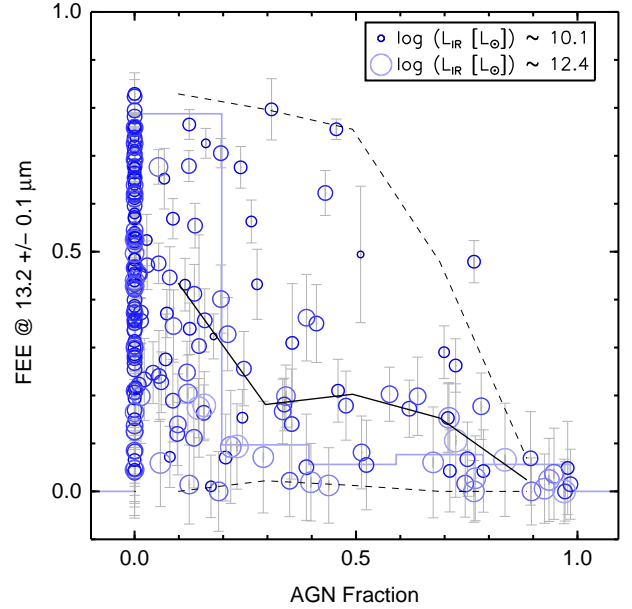


Figure 6. FEE of the $13.2\mu m$ continuum emission as a function of the AGN fraction, estimated by the $6.2\mu m$ PAH equivalent width, for the galaxies of our sample (see Petric et al. 2010). The size of the circles scales with the L_{IR} of the galaxies. The background faint blue line is the normalized histogram of the AGN fraction. The solid black line is the median of the $FEE_{13.2\mu m}$ at the different bins of AGN-fraction. The lower and upper dashed lines are the minimum and maximum $FEE_{13.2\mu m}$ at each bin respectively.

the total, stage 4 $FEE_{13.2\mu m}$ distribution and those of the rest of merging stages yield significance values always lower than 0.01. K-S tests performed among the 0 – 3 merging stage datasets provide significance values between 0.4 and 0.75. This implies that in fact galaxies classified as to be at merging stage 4 are systematically more compact.

Regarding the IR luminosity bin distributions, we see that merging stage 4 systems are not necessarily the most IR luminous only (see also Rigopoulou et al. 1999) but 15% (8/54) have IR luminosities lower than $10^{11.25} L_{\odot}$. On the other hand, we find that the vast majority, 89% (16/18), of ULIRGs are systems classified as mergers in their final stage of interaction and all have $FEE_{13.2\mu m} \leq 0.2$, in agreement with previous findings. Similarly, galaxies at the stage 4 of interaction with $10^{11.25} L_{\odot} \leq L_{IR} < 10^{12} L_{\odot}$ also tend to show lower $FEE_{13.2\mu m}$ values (like ULIRGs) than less luminous systems. LIRGs and less IR luminous systems are spread uniformly in the $FEE_{13.2\mu m}$ versus L_{IR} parameter space up to the merging stage 2 (the histograms are flat within the uncertainties).

3.4. Extended Emission And Presence Of An AGN

Another reason why LIRGs and ULIRGs may appear compact in the MIR is the presence of a dominant AGN. We know that the AGN activity is more prevalent in high IR luminosity systems (e.g., Veilleux et al. 1995, 2009), so we would expect that as the AGN emission starts to dominate the IR energy output of a galaxy, it appears progressively less extended.

For all galaxies in our sample the contribution of

an AGN to their MIR emission has been estimated by Petric et al. (2010) using a number of line and continuum features. We use their estimates of the AGN fraction calculated by means of the so-called ‘‘Laurent diagram’’ (Laurent et al. 2000), which is based on the $15\ \mu\text{m}/5.5\ \mu\text{m}$ continuum and $6.2\ \mu\text{m}$ PAH/ $5.5\ \mu\text{m}$ ratios (see Fig. 3 of Petric et al. 2010). By comparing the data in this parameter space with representative ratios of pure AGN, PDR, and HII regions, it is possible to infer the contribution of these components to the total galaxy emission. In Figure 6 we present the $FEE_{13.2\ \mu\text{m}}$ as a function of this AGN fraction for the 210 galaxies for which it could be derived. The galaxies are again displayed as circles, the size of which scales with their IR luminosity. It is clear that as the AGN fraction approaches unity, the maximum $FEE_{13.2\ \mu\text{m}}$ at the different AGN-fraction bins (upper dashed line) decreases and the galaxies become progressively more compact. In addition, the median $FEE_{13.2\ \mu\text{m}}$ (solid line) also decreases as the AGN fraction increases, although more smoothly. In fact, only 5 out of the 30 AGN-dominated galaxies¹⁶ have $FEE_{13.2\ \mu\text{m}} > 0.2$. Independently of the L_{IR} , it is interesting to see that 60% (15/25) of the AGN-dominated galaxies with $FEE_{13.2\ \mu\text{m}} \leq 0.2$ are in the final stage of interaction, while only 12% (3/25) are in the 3rd, 0 in the 2nd, 20% (5/25) in the 1st and 8% (2/25) in the 0th (see Figure 5).

We have found that galaxies classified as mergers in their final stage of interaction tend to have low $FEE_{13.2\ \mu\text{m}}$ values and, in particular for ULIRGs, $FEE_{13.2\ \mu\text{m}} < 0.2$. We also show now that the fraction of ULIRGs in merging stage 4 that are AGN-dominated is 60% (9/15). The fraction of galaxies with $10^{11.25}\ L_{\odot} \leq L_{\text{IR}} < 10^{12}\ L_{\odot}$ and $FEE_{13.2\ \mu\text{m}} \leq 0.2$ (first $FEE_{13.2\ \mu\text{m}}$ bin in Figure 5, stage 4) that are AGN-dominated is 33% (5/15)¹⁷ while for lower luminosity systems is 33% (1/3). Moreover, the fraction of AGN-dominated galaxies classified as mergers at stage 4 with $FEE_{13.2\ \mu\text{m}} > 0.2$ is 0%, independently of the IR luminosity. That is, *all* AGN-dominated galaxies in the stage 4 of interaction are compact.

3.5. Extended Emission And Presence Of Cold Dust

Independently of the process that dominates the IR emission in galaxies (either an AGN or a starburst), we should expect to observe harder radiation fields and higher dust temperatures within more compact environments. In this section we explore whether the extended emission we detect in the $5 - 15\ \mu\text{m}$ wavelength range, that traces warm small dust grains and molecules, depends on the amount of cold dust of our sources. We first calculate the *IRAS* $\log(f_{60\ \mu\text{m}}/f_{100\ \mu\text{m}})$ color of the galaxies, which is a well known IR broad-band AGN diagnostic (de Grijp et al. 1985), but we find that it does not correlate with the extent of the MIR continuum emission. We also explore whether there is a dependence on the *Spitzer* $\log(f_{24\ \mu\text{m}}/f_{70\ \mu\text{m}})$ and $\log(f_{70\ \mu\text{m}}/f_{160\ \mu\text{m}})$ colors but do not find any clear trend. However, when we plot in Figure 7 the $FEE_{13.2\ \mu\text{m}}$ as a function of the

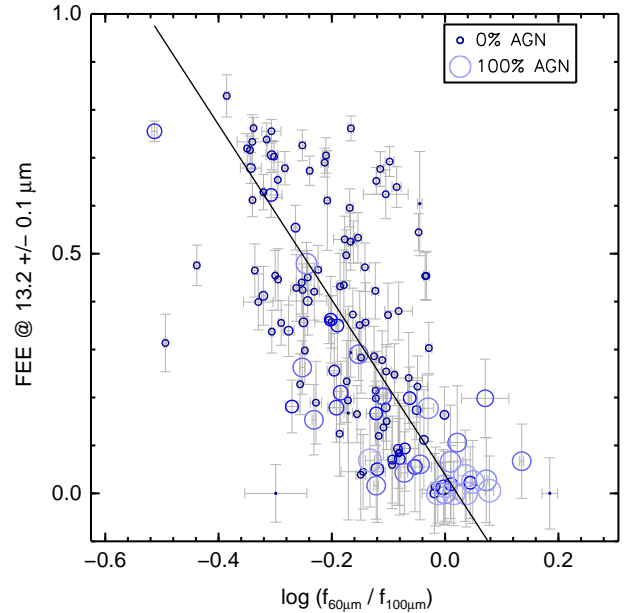


Figure 7. FEE of the $13.2\ \mu\text{m}$ continuum emission as a function of the *IRAS* $\log(f_{60\ \mu\text{m}}/f_{100\ \mu\text{m}})$ color. The sizes of the circles scale with the AGN fraction of the galaxies. Points indicate galaxies for which the AGN-fraction was not available. The solid line is the linear fit to the data.

FIR *IRAS* $\log(f_{60\ \mu\text{m}}/f_{100\ \mu\text{m}})$ color, a correlation is visible. Despite the large scatter, galaxies with cold FIR colors appear to be more extended in their MIR continuum. The Spearman rank correlation coefficient is -0.67 with a significance level of effectively 0, while the Kendall test provides a value of -0.49 , implying that the correlation is real. We fitted our data with an outlier-resistant linear fit algorithm provided by the IDL function `ROBUST_LINEFIT`¹⁸, and the best fit parameters are given in the following equation:

$$FEE_{13.2\ \mu\text{m}} = 0.04 \pm 0.02 - (1.83 \pm 0.11) \times \log\left(\frac{f_{60\ \mu\text{m}}}{f_{100\ \mu\text{m}}}\right) \quad (2)$$

where $FEE_{13.2\ \mu\text{m}}$ is the fraction of the extended emission of a given galaxy at $13.2\ \mu\text{m}$, and $f_{60\ \mu\text{m}}$ and $f_{100\ \mu\text{m}}$ are the *IRAS* flux densities (f_{ν}) at 60 and $100\ \mu\text{m}$, respectively. The data have a scatter of 0.2 in the y-axis and 0.1 in the x-axis. The uncertainties in the parameters of the fit have been calculated using bootstrapping resampling analysis. In order to avoid interacting systems for which only one *IRAS* color has been measured due to the limited spatial resolution, we have used only 142 sources for which there is a unique association between one galaxy (one $FEE_{13.2\ \mu\text{m}}$ measurement) and one *IRAS* color. In addition to this correlation, Figure 7 also shows that nearly all galaxies whose MIR emission is dominated by an AGN (i.e., they have a high AGN fraction according to the estimates of Petric et al. 2010) are located at the lower right corner of the plot, which means that they are more compact, and have warmer FIR colors. Even if

¹⁶ We define as AGN-dominated galaxies those that have an AGN fraction larger than 0.5.

¹⁷ We have AGN classification for 15 out of 16 galaxies in each of the ULIRG and $10^{11.25}\ L_{\odot} \leq L_{\text{IR}} < 10^{12}\ L_{\odot}$ luminosity bins.

¹⁸ The procedure `ROBUST_LINEFIT.PRO` can be found in http://spectro.princeton.edu/goddard_doc.html

we exclude AGN dominated systems and consider only starburst galaxies with an AGN fraction close to zero, the correlation is still present.

This result has an interesting implication for the forthcoming studies of the cold dust emission of LIRGs/ULIRGs with the *Herschel Space Telescope*. Figure 7 suggests that “cold” FIR-selected (U)LIRGs will likely present large $FEE_{13.2\mu m}$ values. As a result one would expect that a large fraction of their MIR continuum emission originates in their extended component (see previous section). Furthermore, based on the study by Bothun & Rogers (1992), the *IRAS* $\log(f_{60\mu m}/f_{100\mu m})$ colors of our galaxies suggest that they have very strong dust temperature gradients (their Section 4.1 and Table 3). Consequently the cold, FIR emission from these systems will be more extended than the warmer MIR emission. Taking this into account, the FEE we derive for the MIR continuum emission based on our *Spitzer*/IRS observations places a lower limit to the extent of the FIR continuum emission. Therefore, despite the limitations of our long-slit MIR spectra, one may obtain a rough estimate on how much of the FIR emission is extended in any LIRG/ULIRG.

3.6. Implications For High-Redshift SMGs

By virtue of the negative K -correction, SMGs are systems with IR luminosities in the ULIRG range, almost independently of their redshift. Recent studies of SMGs, based on various diagnostics including the MIR and FIR wavelength range have suggested that they are systems dominated by star formation (Pope et al. 2008; Farrah et al. 2008; Murphy et al. 2009; Sajina et al. 2007, 2008, 2009). In addition, interferometric observations of their CO content and radio continuum emission reveal that they host large amounts of dust and molecular gas ($M_{H_2} \sim 10^{10-11} M_{\odot}$) which may fuel prodigious star formation rates of several hundred solar masses per year (Neri et al. 2003; Chapman et al. 2004; Greve et al. 2005; Daddi et al. 2009a, b; Tacconi et al. 2008). Analysis of the kinematics of their ionized gas emission using the $H\alpha$ emission red-shifted in the near-infrared, indicate that SMGs as well as some high-redshift ULIRGs are extended up to several kpc scales (e.g., Alexander et al. 2010). In some cases they display motions which can be attributed to organized rotating disks and in others they appear to belong to interacting systems (Tacconi et al. 2008; Bothwell et al. 2010; Ivison et al. 2010). Recent studies of the FIR continuum and [CII] $158\mu m$ emission of high- z IR luminous galaxies also suggest that the star formation in these sources is extended over several kpc (Kovács et al. 2010; Hailey-Dunsheath et al. 2010).

It is well accepted that in the local universe the MIR emission traces the star formation regions emitting in $H\alpha$ and it correlates with the presence of molecular gas. Based on our analysis we find no evidence that the local ULIRGs of the GOALS sample are extended in the MIR to the sizes suggested by the $H\alpha$ or CO measurements of high- z sources. It is true that the *Spitzer* spatial resolution is quite limited, but we have shown that even the closest ULIRGs in our sample have unresolved cores and $FEE_{13.2\mu m} \lesssim 0.2$. Instead it is the LIRG population that displays resolved emission extended over several kpc scales. In addition, it appears that the SMG population comprises not only isolated, disk-like galaxies but

also merging systems, which is also in agreement with our findings for the LIRG class.

On the other hand, it is still uncertain whether high-redshift IR luminous sources are simple scaled up analogues of local, less luminous systems in terms of all their physical properties. Integrated MIR spectra of SMGs (Pope et al. 2008; Menéndez-Delmestre et al. 2009) do display PAH equivalent widths more typical of local LIRGs rather than the weaker values found for local ULIRGs (Desai et al. 2007). However, some recent works suggest that the star formation law in SMGs is similar to that of local ULIRGs and is much more efficient than in local, less IR luminous disk-like galaxies, or than in high- z BzK galaxies (Daddi et al. 2010a; Daddi et al. 2010b; Genzel et al. 2010). We will address the issue of the spectral properties of star formation in local LIRGs and ULIRGs in our next paper, where we analyze separately the nuclear and extended emission of the PAH features, emission lines and the $9.7\mu m$ silicate feature of the galaxies in the GOALS sample.

4. CONCLUSIONS

We analyzed the spatial profiles of low-resolution $5-15\mu m$ *Spitzer*/IRS spectra of the GOALS sample and quantified the extent of their MIR emission, FEE_{λ} . Our work indicates that:

- There is a diversity in the shape of the FEE_{λ} as a function of wavelength. The variation in the spatial extent of the various MIR features such as PAHs, emission lines, and continuum implies that the MIR emission in (U)LIRGs is complex. However, we find 3 types of FEE_{λ} functions: constant/featureless, PAH-/line-extended, and silicate-extended. Several physical processes, such as AGN emission as well as multiple bursts of star formation, nuclear and extra-nuclear, are suggested to produce the integrated MIR spectrum of (U)LIRGs and to determine their spatial extent at different wavelengths.
- More than 90% of the galaxies in the GOALS sample have median FEE_{λ} larger than 0.1. Furthermore, more than 30% of the galaxies have median FEE_{λ} larger than 0.5, implying that at least half of their MIR emission is extended. As a whole, the median FEE_{λ} of local LIRGs is $\sim 2-3$ times larger than that of ULIRGs.
- Despite the limited spatial resolution of the *Spitzer*/IRS spectra, we find a steep decrease in the extent of the continuum emission, $FEE_{13.2\mu m}$, at the threshold of $L_{IR} \sim 10^{11.8} L_{\odot}$. While LIRGs display a wide range of $FEE_{13.2\mu m}$, spanning from compact objects to sources extended up to 85%, galaxies above this threshold show unresolved cores and very compact emission, in particular ULIRGs, which all have $FEE_{13.2\mu m} \lesssim 0.2$ independently of their distance. We measure galaxy core sizes (FWHMs) of LIRGs at $13.2\mu m$ up to 10 kpc, with a mean of 2.6 kpc if upper limits to the sizes of unresolved galaxies are taken into account. If only resolved sources are considered, the mean core size of LIRGs is 3.1 kpc. Our estimate for those of ULIRGs is less than 1.5 kpc.

- Galaxies classified as mergers in their final stage of interaction, based on imaging from the *Hubble* and *Spitzer Space Telescopes*, show lower $FEE_{13.2\mu\text{m}}$ values than galaxies in earlier stages. Galaxies with $10^{11.25} L_{\odot} \leq L_{\text{IR}} < 10^{12} L_{\odot}$ in their final stage of interaction also display a similar trend (like ULIRGs), showing lower $FEE_{13.2\mu\text{m}}$ values than less luminous systems.
- The maximum and the median $FEE_{13.2\mu\text{m}}$ decrease as the AGN-fraction increases. Galaxies with AGN-fractions larger than 50% are more compact, and 60% of those that have $FEE_{13.2\mu\text{m}} < 0.2$ are systems in the final stage of interaction. Furthermore, *all* AGN-dominated galaxies classified as mergers in their final stage of interaction have $FEE_{13.2\mu\text{m}} < 0.2$, i.e., are compact, independently of their L_{IR} .
- The $FEE_{13.2\mu\text{m}}$ and the *IRAS* $\log(f_{60\mu\text{m}}/f_{100\mu\text{m}})$ color appear to be correlated, with the MIR continuum emission of colder galaxies being more extended. Due to the large temperature gradients present in our galaxies, the FEE of the MIR con-

tinuum provides a rough lower limit to the FEE of the FIR emission in these systems.

Determining the extent of a galaxy at MIR, FIR, and even radio wavelengths can yield information about how the stellar populations are distributed in it, and therefore reveal how the galaxy has formed and evolved. These questions will be soon addressed by new observations obtained with the *Herschel Space Telescope* and the Atacama Large Millimeter Array (ALMA), and in the more distant future with the *James Webb Space Telescope*.

TD-S wants to thank E. da Cunha for her suggestions and interesting discussions. TD-S and VC would like to acknowledge partial support from the EU ToK grant 39965 and FP7-REGPOT 206469. This research has made use of the NASA/IPAC Extragalactic Database (NED), which is operated by the Jet Propulsion Laboratory, California Institute of Technology, under contract with the National Aeronautics and Space Administration, and of NASA’s Astrophysics Data System (ADS) abstract service.

APPENDIX

OBTAINING THE FEE_{λ} FUNCTIONS

Detailed Data Reduction and Calculation of the FEE_{λ}

In order to calculate the fraction of extended emission (FEE_{λ}) as a function of wavelength, we used as input data the 2 dimensional IRS coa2ds files obtained as explained in Petric et al. (2010). Due to the limited spatial resolution of *Spitzer*, we performed the analysis using only the SL module (see Section 2.2), which covers a wavelength range from $\sim 5.5\mu\text{m}$ to $\sim 14.5\mu\text{m}$ (SL2 order: $\sim 5.5\mu\text{m}$ to $\sim 7.5\mu\text{m}$; SL1 order: $\sim 7.5\mu\text{m}$ to $\sim 14.5\mu\text{m}$). Details regarding the steps taken for the reduction and creation of the coa2ds can be found in Petric et al. (2010). We used version 18.7 of the *wavesamp* file which contains the information on the projection of the spatial and spectral elements of the IRS slits onto the 2 dimensional detector array via a set of pseudo-rectangles. Each pseudo-rectangle defines the spatial direction that crosses an IRS spectrum at a given wavelength. Therefore, to extract the spatial profiles of a galaxy as a function of wavelength, we interpolated the IRS spectrum along the direction traced by each pseudo-rectangle. The same approach was taken to produce the spatial profiles of the standard star used as our reference point spread function (PSF) representing an unresolved source. Each spatial profile was fitted with a Gaussian function leaving as free parameters its maximum intensity, position, and full width half maximum (FWHM). Indeed, the later gives us a measure of the size of the source’s “core” at each wavelength (i.e., the Gaussian component of the extended emission; see Figure 4b). To calculate the unresolved emission of the galaxy, we scaled the maximum of the PSF spatial profile to the maximum of the galaxy spatial profile and subtracted it. The remaining flux is the extended emission (EE) of the galaxy. We also measured the total emission of the galaxy by integrating the flux over the entire spatial profile defined by the IRS slit. The EE divided by the total emission of the galaxy is the fraction of EE (FEE). This calculation was repeated for each wavelength resolution element (pseudo-rectangle) and consequently the FEE is a function of λ (FEE_{λ}). The calculation of the FEE_{λ} has some advantages over other methods used to ascertain the compactness of a galaxy, such as the concentration index or the Gini coefficient. The concentration index relies on aperture photometry and therefore does not provide an estimate the shape of the spatial distribution of the PSF, mixing both unresolved and resolved emission. The Gini coefficient is also totally independent of the shape of the galaxy. As a consequence the growth of the physical size of the unresolved component of the galaxy with distance is not taken into account and it is intrinsically included in the Gini statistics, which would make the interpretation of our results even more challenging.”

Corrections to the FEE_{λ}

Since the pixel size of the IRS SL detector is $1.8'' \times 1.8''$, the IRS spectra are under-sampled below $\sim 10\mu\text{m}$. The under-sampling affects the spatial distribution of the flux of unresolved sources over the pixels of the detector. As a result, the exact pixel intensity depend on where the source is located on it at a sub-pixel scale. Since a IRS spectrum does not run along the columns of the detector but it displays a slight curvature, the spatial profile of the source at each spectral resolution element is not centered at the same sub-pixel position for all wavelengths. Therefore the under-sampling introduces an intrinsic variation on the shape of the spatial profiles as a function of the wavelength, which is reflected in a change of the FWHM as well as the maximum value of the fitted Gaussian to the spatial profiles. The effect of the under-sampling can be seen in Figure 8 where the FWHM and maximum of the spatial profiles of

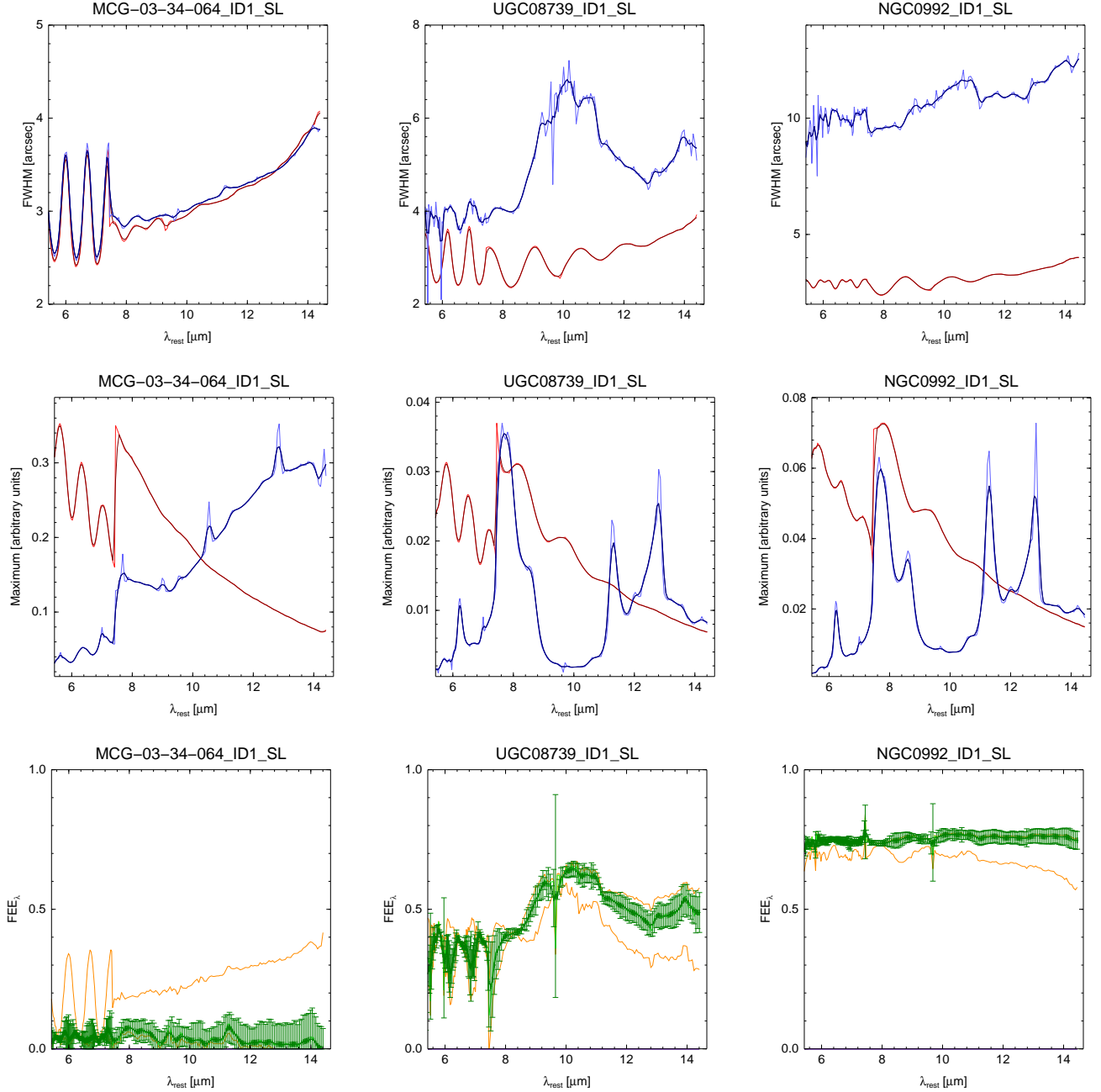


Figure 8. Top panel: FWHM of the Gaussian function for three galaxies of the sample as a function of wavelength and averaged for the two nod positions (blue lines). The FWHM of the PSF is also shown for reference (red lines). The galaxy on the left is unresolved while the other two show FWHMs larger than those of the PSF. Middle panel: Maximum of the Gaussian function (arbitrary scaled) for the same three galaxies as a function of wavelength and averaged for the two nod positions (blue lines). These plots are equivalent to the spectra of the galaxies, except that they are affected by the under-sampling. The maximum of the PSF (arbitrary scaled at each order) is also plotted for reference (red lines). Bottom panel: Fraction of extended emission, FEE_{λ} , for the same three galaxies as function of the wavelength and averaged for the two nod positions (green lines). The bottom orange lines represent the FEE_{λ} that would be obtained if the correction factor was not applied at all, that is, if we considered that the source is totally unresolved. The top orange lines represent the FEE_{λ} that would be obtained if the correction factor was fully applied, that is, if we considered that the source is very extended. See text for details. The thin-colored lines are actual values. The thick-colored lines are the same values but smoothed with a 4-pixel box to reduce the noise.

the PSF are shown as a function of the wavelength (red lines; top and middle panels). We note that the FWHM and maximum may vary as much as 50% in the SL2 module. This factor is very important because, in order to calculate the amount of extended emission of a galaxy at a given wavelength, we need to scale the maximum of the PSF to the maximum of the profile of our source. If a galaxy is unresolved, its fitted maximum will present the same behavior as the maximum of the PSF and the wiggling pattern created by the under-sampling will cancel out. If, on the contrary, a galaxy is resolved, its spatial profile will not be affected by the under-sampling, but the profile of our PSF will be and will introduce this pattern in the calculation of the FEE_λ .

Therefore, before the calculation of the FEE_λ of a galaxy, we need to correct the maximum of the PSF, in a manner which takes into account the under-sampling in the spatial profile of the galaxy, which in turn depends on its compactness. In order to calculate how compact the galaxy is, we compare its fitted FWHM with that of the unresolved PSF at each wavelength and correct accordingly the maximum of the PSF. A zero correction means that the galaxy is totally unresolved, as is the PSF. A full correction is applied when the galaxy is much more extended than the PSF and implies that we have to correct the maximum of the PSF as if it was not affected by the under-sampling at all. What is this correction factor?

The correction factor to the maximum of the PSF is the value of the FWHM of the PSF normalized to its real value at the same wavelength. This is because even if the FWHM and the maximum of the spatial profile of an unresolved source oscillates as a function of the wavelength due to the under-sampling, the total flux does not. As a consequence, the patterns of the FWHM and the maximum of the PSF are “synchronized” (the maximum of one is the minimum of the other; see Figure 8, top and middle panels, red lines) and thus we can use the value of the FWHM to correct the maximum to its real value. In this we assume that the “real” (highest) spatial resolution that can be achieved at a given wavelength is the one defined by the minimum of the lower envelope showed by the pattern of the FWHM function of the PSF. Values larger than this are affected by the under-sampling and cause the FWHM of the spatial profiles to be over-estimated and, conversely, the maximum to be under-estimated. Therefore, in order to correct for the under-sampling, we multiply the maximum of the PSF by the ratio of its observed-to-minimum (real) FWHM. As we mentioned above, this correction depends on how resolved a galaxy is. In unresolved sources the correction is not necessary, while in very extended galaxies it needs to be fully applied. In order to demonstrate the success and accuracy of the method, in Figure 8 we show the FWHM, maximum and FEE_λ function of 3 galaxies resolved in a different degree. The final FEE_λ at a given wavelength is the average of the values obtained for each one of the two nod positions of the IRS slits, and the uncertainty is the difference between both.

We can see that the FEE_λ function (bottom panel, green line), once corrected for the under-sampling effect, shows almost no residuals of the wiggling pattern that can be seen in the FWHM and maximum functions (top and middle panels) of the galaxies and the PSF. Furthermore, the correction works very well for almost unresolved sources (left panels), very extended sources (right panels), as well as for intermediate-resolved sources (center panels). As an example, we show in the bottom panels, together with the FEE_λ function (in green), the FEE_λ function that would have been obtained if we had not applied the correction factor at all (lower orange line) or if it had been fully applied (top orange line), that is if we had not taken into account the *a priori* knowledge on how extended our galaxy is. The comparison of the FWHMs of the galaxy and the PSF is therefore essential in order to know to which extent the correction factor must be applied at a given wavelength. This is specially true for galaxies that are slightly resolved at certain wavelengths, as is the case of UGC 08739 (middle panel).

There were a few cases, however, where an accurate FEE_λ function could not be accurately recovered for the SL2 order (IC 4734, ESO 279-G011, MCG-02-33-098, CGCG 468-002 and MCG-05-12-006). These are galaxies that show FWHM functions that do not present a wiggling pattern despite they are almost unresolved. Therefore their FEE_λ functions from $\sim 5.5 \mu\text{m}$ to $\sim 7.5 \mu\text{m}$ are very uncertain.

Additional Tests

In addition, we checked whether the FEE as a function of the wavelength obtained with the IRS spectra is consistent with the value that can be calculated from the IRAC images at $8 \mu\text{m}$. To do so we performed a PSF-fitting analysis to the images in the same way as we did for the spatial profiles of the IRS spectra at each wavelength. First, we used a sub-sampled point response function (PRF) for the $8 \mu\text{m}$ IRAC band-pass provided by the SSC and interpolated it to the sub-pixel position in the image where the galaxy was located. Then, we rebinned the PRF to the pixel size of the IRAC mosaic, scaled it to the peak of the emission of the galaxy, and subtracted the unresolved emission represented by this scaled-PRF. Finally we measured the remaining flux in an area approximately equal to that used for measuring the integrated emission of the galaxy in the IRS slit (see Section 2.4). Using Equation 1 as for the spectroscopy, the $FEE_{8 \mu\text{m}}$ obtained from the IRAC $8 \mu\text{m}$ imaging is the ratio of the remaining emission to the total integrated emission of the galaxy measured in the same aperture.

There are some cases where the $FEE_{8 \mu\text{m}}$ is greater the FEE calculated from the IRS spectra. This is due to the different surfaces used for measuring the emission of the galaxy in each case (for imaging and spectroscopy). Although both apertures have the same area, the former has the shape of a box while the one of the IRS slit is very elongated. Since, as it is said above, the slit was not oriented in a preferred direction over the galaxies, a boxy-shaped aperture used for measuring the emission will generally lead to a higher FEE because of its symmetry around the central region of the galaxy which in many cases is axisymmetric. Therefore, the fact that the $FEE_{8 \mu\text{m}}$ is slightly above than those calculated using the IRS data for some galaxies is totally consistent with the approach taken and shows that both calculations of the FEE , using imaging and spectroscopy, are in agreement.

REFERENCES

- Alexander, D. M., Swinbank, A. M., Smail, I., McDermid, R., & Nesvadba, N. P. H. 2010, *MNRAS*, 402, 2211
- Armus, L., et al. 2007, *ApJ*, 656, 148
- , 2009, *PASP*, 121, 559
- Bothun, G. D., & Rogers, C. 1992, *AJ*, 103, 1484
- Bothwell, M. S., et al. 2010, *MNRAS*, 405, 219
- Brandl, B. R., et al. 2006, *ApJ*, 653, 1129
- Bryant, P. M., & Scoville, N. Z. 1999, *AJ*, 117, 2632
- Caputi, K. I., et al. 2007, *ApJ*, 660, 97
- Chapman, S. C., Smail, I., Windhorst, R., Muxlow, T., & Ivison, R. J. 2004, *ApJ*, 611, 732
- Clements, D. L., Sutherland, W. J., McMahon, R. G., & Saunders, W. 1996, *MNRAS*, 279, 477
- Daddi, E., et al. 2009a, *ApJ*, 694, 1517
- , 2010a, *ApJ*, 713, 686
- , 2010b, *ApJ*, 714, L118
- de Grijp, M. H. K., Miley, G. K., Lub, J., & de Jong, T. 1985, *Nature*, 314, 240
- Desai, V., et al. 2007, *ApJ*, 669, 810
- Díaz-Santos, T., Alonso-Herrero, A., Colina, L., Packham, C., Levenson, N. A., Pereira-Santaella, M., Roche, P. F., & Telesco, C. M. 2010, *ApJ*, 711, 328
- Díaz-Santos, T., Alonso-Herrero, A., Colina, L., Packham, C., Radoski, J. T., & Telesco, C. M. 2008, *ApJ*, 685, 211
- Downes, D., & Solomon, P. M. 1998, *ApJ*, 507, 615
- Farrar, D., et al. 2008, *ApJ*, 677, 957
- Fazio, G. G., et al. 2004, *ApJS*, 154, 10
- Genzel, R., et al. 2010, *ArXiv e-prints*
- Greve, T. R., et al. 2005, *MNRAS*, 359, 1165
- Haan et al., S. 2010, *ApJ*, submitted
- Hailey-Dunsheath, S., Nikola, T., Stacey, G. J., Oberst, T. E., Parshley, S. C., Benford, D. J., Staguhn, J. G., & Tucker, C. E. 2010, *ApJ*, 714, L162
- Houck, J. R., et al. 1984, *ApJ*, 278, L63
- , 2004, *ApJS*, 154, 18
- , 2005, *ApJ*, 622, L105
- Imanishi, M., Nakagawa, T., Ohshima, Y., Shirahata, M., Wada, T., Onaka, T., & Oi, N. 2008, *PASJ*, 60, 489
- Ivison, R. J., Smail, I., Papadopoulos, P. P., Wold, I., Richard, J., Swinbank, A. M., Kneib, J., & Owen, F. N. 2010, *MNRAS*, 404, 198
- Kovács, A., et al. 2010, *ArXiv e-prints*
- Laurent, O., Mirabel, I. F., Charmandaris, V., Gallais, P., Madden, S. C., Sauvage, M., Vigroux, L., & Cesarsky, C. 2000, *A&A*, 359, 887
- Le Floch, E., Charmandaris, V., Laurent, O., Mirabel, I. F., Gallais, P., Sauvage, M., Vigroux, L., & Cesarsky, C. 2002, *A&A*, 391, 417
- Le Floch, E., et al. 2005, *ApJ*, 632, 169
- Mazzarella, J. M., & et al. 2010, *ApJ*, in preparation
- Menéndez-Delmestre, K., et al. 2009, *ApJ*, 699, 667
- Murphy, E. J., Chary, R., Alexander, D. M., Dickinson, M., Magnelli, B., Morrison, G., Pope, A., & Teplitz, H. I. 2009, *ApJ*, 698, 1380
- Murphy, Jr., T. W., Soifer, B. T., Matthews, K., & Armus, L. 2001, *ApJ*, 559, 201
- Neri, R., et al. 2003, *ApJ*, 597, L113
- Pereira-Santaella, M., Alonso-Herrero, A., Rieke, G. H., Colina, L., Díaz-Santos, T., & et al. 2010, *ApJ*, in press
- Pérez-González, P. G., et al. 2005, *ApJ*, 630, 82
- Petric et al., A. O. 2010, *ApJ*, submitted
- Pope, A., et al. 2008, *ApJ*, 675, 1171
- Rieke, G. H., et al. 2004, *ApJS*, 154, 25
- Rigby, J. R., et al. 2008, *ApJ*, 675, 262
- Rigopoulou, D., Spoon, H. W. W., Genzel, R., Lutz, D., Moorwood, A. F. M., & Tran, Q. D. 1999, *AJ*, 118, 2625
- Sajina, A., Spoon, H., Yan, L., Imanishi, M., Fadda, D., & Elitzur, M. 2009, *ApJ*, 703, 270
- Sajina, A., Yan, L., Armus, L., Choi, P., Fadda, D., Helou, G., & Spoon, H. 2007, *ApJ*, 664, 713
- Sanders, D. B., Mazzarella, J. M., Kim, D.-C., Surace, J. A., & Soifer, B. T. 2003, *AJ*, 126, 1607
- Sanders, D. B., & Mirabel, I. F. 1996, *ARA&A*, 34, 749
- Soifer, B. T., & Neugebauer, G. 1991, *AJ*, 101, 354
- Soifer, B. T., et al. 2000, *AJ*, 119, 509
- , 2001, *AJ*, 122, 1213
- Spoon, H. W. W., et al. 2004, *ApJS*, 154, 184
- Surace, J. A. 1998, PhD thesis, Institute for Astronomy University of Hawaii 2680 Woodlawn Dr. Honolulu, HI 96822
- Tacconi, L. J., et al. 2008, *ApJ*, 680, 246
- Veilleux, S., Kim, D.-C., Sanders, D. B., Mazzarella, J. M., & Soifer, B. T. 1995, *ApJS*, 98, 171
- Veilleux, S., et al. 2009, *ApJS*, 182, 628
- Werner, M. W., et al. 2004, *ApJS*, 154, 1
- Yan, L., et al. 2005, *ApJ*, 628, 604